

# THE HI PARKES ZONE OF AVOIDANCE SURVEY: THE NORTHERN EXTENSION

J. L. DONLEY,<sup>1,2</sup> L. STAVELEY-SMITH,<sup>1</sup> R. C. KRAAN-KORTEWEG,<sup>3</sup> J. M. ISLAS-ISLAS,<sup>3</sup> A. SCHRÖDER,<sup>4</sup> P. A. HENNING,<sup>5</sup> B. KORIBALSKI,<sup>1</sup> S. MADER,<sup>1</sup> AND I. STEWART<sup>4</sup>

*Accepted for publication in The Astronomical Journal (January 2005 issue)*

## ABSTRACT

We present the results of the northern extension of the HI Parkes Zone of Avoidance Survey, a blind HI survey utilizing the multibeam receiver on the Parkes 64-m telescope. In the two regions studied here,  $l = 36^\circ$  to  $52^\circ$  and  $l = 196^\circ$  to  $212^\circ$ ,  $|b| \leq 5^\circ$ , we have detected 77 HI galaxies, twenty of which have been previously detected in HI. The survey has a median rms noise of  $6.0 \text{ mJy beam}^{-1}$  and is complete to a mean flux density of  $22 \text{ mJy}$ . We have searched for multiwavelength counterparts to the 77 galaxies detected here: 19, 27, and 11 have a likely optical, 2MASS, and IRAS cataloged counterpart, respectively. A further 16 galaxies have likely visible counterparts on the Digitized Sky Survey. The detection of these 77 galaxies allows a closer inspection of the large-scale structures in these regions. We see several filaments crossing the Galactic plane, one of which appears to be the continuation of a sine-wave like feature that can be traced across the whole southern sky. An analysis of the HI mass function suggests that the regions studied here may be underdense. One particularly noteworthy galaxy is HIZOA J0630+08 ( $l, b = 203^\circ, -0.9^\circ$ ) with a velocity of  $367 \pm 1 \text{ km s}^{-1}$ . We suggest that it belongs to the nearby Orion Group which includes a small number of dwarf galaxies. The newly detected galaxies improve our understanding of the properties of several voids, such as the Orion, Gemini, and Canis Major Voids.

*Subject headings:* galaxies: distances and redshifts — galaxies: fundamental parameters — large-scale structure of universe — surveys

## 1. INTRODUCTION

The obscuring effects of dust and high stellar density in the Milky Way have historically prevented the detection of galaxies that lie behind the disk of our Galaxy. This zone of avoidance (ZOA) typically comprises more than 20% of the optical extragalactic sky and nearly 10% of the infrared extragalactic sky, although recent surveys have begun to lessen its extent. The presence of the ZOA does not affect extragalactic population studies, as galaxies in the highly obscured ZOA should not differ from those detected in regions of low obscuration. A complete census of galaxies across the Galactic plane is necessary, however, to fully understand the dynamics of the Local Group as well as the large-scale structure of the Local Universe.

Many early ZOA studies focused on finding a highly obscured, nearby, massive galaxy. Several such galaxies have been found, including Maffei 1 and 2 (Maffei 1968), Circinus (Freeman et al. 1977), and Dwingeloo 1 (Kraan-Korteweg et al. 1994). While the IC 342/Maffei group and other nearby massive galaxies largely define the motion of the Local Group, the direction of the Local Group acceleration is strongly affected by the full ZOA mass distribution out to  $6000 \text{ km s}^{-1}$  (Kolatt, Dekel, & Lahav 1995), and possibly beyond.

Several attempts have been made in recent years to sample the ZOA more completely. Optical galaxy candidates have been identified by searches of the Palomar Observatory Sky Survey (POSS) prints and Schmidt atlases (see Kraan-Korteweg & Lahav 2000 for a review). Highly obscured galaxies have also been detected in the near-infrared (NIR) and far-infrared by the Deep Near-Infrared Survey of the Southern Sky (DENIS; Schröder, Kraan-Korteweg, & Mamon 1999), the Two Micron All Sky Survey (2MASS; Jarrett et al. 2000), and the Infrared Astronomical Satellite Sky Survey (IRAS, e.g. Nakanishi et al. 1997).

While useful in reducing the size of the ZOA, optical and infrared surveys are ultimately limited by Galactic extinction and source confusion. The most thorough optical searches are complete to an apparent diameter of  $D = 14''$  and a magnitude of  $B_{25} = 18^m.5$  at extinctions of  $A_B \leq 3^m.0$  (Kraan-Korteweg 2000, Woudt & Kraan-Korteweg 2001). The DIRBE/IRAS  $100 \mu\text{m}$  extinction maps (Schlegel, Finkbeiner, & Davis 1998) directly measure the dust column density and indicate that  $A_B \geq 3^m.0$  for 9.5% of the sky, although the data in the Galactic plane are not yet well-calibrated. The completeness of infrared surveys of the ZOA is affected primarily by source confusion. Results from the DENIS survey indicate that NIR surveys can easily detect galaxies down to  $A_B \sim 10 \text{ mag}$ , and the brighter ones far beyond (Schröder et al. 1999). The 2MASS survey is expected to be complete to  $13^m.5$  at  $2.2 \mu\text{m}$  for the majority of the sky, but for  $5^\circ \leq |b| \leq 20^\circ$ , this completeness drops to  $12^m.1$  (Jarrett et al. 2000).

HI emission is not affected by the dust in the Milky Way. Consequently, blind HI surveys provide a unique means by which to identify gas-rich ZOA galaxies. The first blind ZOA HI survey was conducted by Henning (1992) using the Green Bank 300-ft telescope. More recent blind HI surveys include the Arecibo Dual Beam Survey (ADBS, Rosenberg & Schneider 2000) and the Arecibo HI Strip Survey (AHISS, Zwaan et al. 1997), which intersect with but do not focus on the ZOA.

<sup>1</sup> Australia Telescope National Facility, CSIRO, P.O. Box 76, Epping, NSW 1710, Australia; Lister.Staveley-Smith@csiro.au, Baerbel.Koribalski@csiro.au, Stacy.Mader@csiro.au

<sup>2</sup> Steward Observatory, University of Arizona, 933 North Cherry Avenue, Tucson, AZ 85721; jdonley@as.arizona.edu

<sup>3</sup> Departamento de Astronomía, Universidad de Guanajuato, Apdo. Postal 144, Guanajuato, GTO 36000, Mexico; kraan@astro.ugto.mx, jmislas@astro.ugto.mx

<sup>4</sup> Department of Physics and Astronomy, University of Leicester, Leicester LE1 7RH, UK; acs@star.le.ac.uk, ims@star.le.ac.uk

<sup>5</sup> Institute for Astrophysics, University of New Mexico, 800 Yale Boulevard, NE, Albuquerque, NM 87131; henning@cosmos.phys.unm.edu

The first systematic HI survey to focus on the optically most opaque part of the ZOA is the Dwingeloo Obscured Galaxies Survey (Henning et al. 1998, Rivers 2000) which sampled the northern ZOA ( $30^\circ \leq l \leq 220^\circ$ ,  $|b| \leq 5^\circ.25$ ) to velocities of  $4000 \text{ km s}^{-1}$  in the Local Group standard of rest with an rms of  $40 \text{ mJy beam}^{-1}$ . Each of these surveys has contributed to our understanding of gas-rich galaxies and the structure of the local Universe, but all have been limited in either sensitivity or sky coverage.

The 21-cm multibeam receiver (Staveley-Smith et al. 1996) on the Parkes<sup>6</sup> 64-m telescope is the first instrument capable of conducting both sensitive *and* large-area blind HI surveys in a reasonable time. Two multibeam surveys commenced in 1997. The HI Parkes All-Sky Survey (HIPASS, see Meyer et al. 2004) is a blind HI survey of the sky south of  $\delta = 25^\circ$  and has an rms noise of  $13 \text{ mJy beam}^{-1}$ . The HI Parkes Zone of Avoidance Survey is a more sensitive (rms =  $6 \text{ mJy beam}^{-1}$ ) survey of the region of the Milky Way accessible from Parkes ( $l = 196^\circ$  to  $52^\circ$ ,  $|b| < 5^\circ$ ). An analysis of shallower data for the southern ZOA (rms =  $15 \text{ mJy beam}^{-1}$ ,  $l = 212^\circ$  to  $36^\circ$ ) led to the discovery of 110 galaxies, 67 of which were previously unknown (Henning et al. 2000). Here we report on the results for the complementary region north of Dec.  $0^\circ$  ( $l = 36^\circ$  to  $52^\circ$  and  $l = 196^\circ$  to  $212^\circ$ ). The results reported here are, however, at full survey sensitivity (rms =  $6 \text{ mJy beam}^{-1}$ ). Although this region overlaps with the Dwingeloo survey, the Parkes survey is much more sensitive and represents the first probe, beyond a few Mpc, of this region of the Universe, which lies near both the Local and Microscopium Voids. Data of similar depth for the remainder of the ZOA ( $l = 212^\circ$  to  $36^\circ$ ) will be reported elsewhere.

In §2, we describe the observations and the method by which the data were reduced. The galaxy search method, measurement of HI parameters, search results, and survey completeness are discussed in §3. In §4, we describe the results of a search for multiwavelength counterparts to the survey galaxies. The large-scale structures revealed by the survey are discussed in §5, and the mass function of the galaxies is discussed in §6. Throughout the paper, we assume  $H_0 = 75 \text{ km s}^{-1} \text{ Mpc}^{-1}$ .

## 2. OBSERVATIONS AND DATA REDUCTION

The observations for the northern extension of the HI Parkes ZOA survey began in 2000 October and were completed in 2002 May. The data were taken at the Parkes 64-m telescope using the 21-cm multibeam receiver, which consists of an array of 13 beams each with two orthogonal linear polarizations and an average beamwidth of  $14'.3$  (FWHM). The multibeam correlator has a bandwidth of 64 MHz and covers the velocity range  $-1200 < cz < 12700 \text{ km s}^{-1}$ . The channel spacing is  $13.2 \text{ km s}^{-1}$  and the average system temperature is 20K.

The northern ZOA region referred to in this paper lies at declinations  $\gtrsim 0^\circ$  and is divided into four fields, each approximately  $8^\circ \times 10^\circ$ , as shown in Figure 1. Each field was scanned 425 times, with a single  $8^\circ$  scan covering a region  $1.7^\circ$  wide in eight minutes. The central beam for all scans lies along a line of constant Galactic latitude, with each of the 425 scans being separated by  $1'.4$  in latitude. At the midpoint of each scan, the feed angle is  $15^\circ$  with respect to the scan direction so that all

13 beams lie at different latitudes in a minimally redundant fashion. The total integration time is  $2100 \text{ s beam}^{-1}$ . The median rms noise of the four fields after Hanning smoothing is  $6.0 \text{ mJy beam}^{-1}$ .

The data were bandpass-corrected, Doppler-corrected, and calibrated using AIPS++ LIVEDATA (Barnes et al. 2001). Gridding was performed by GRIDZILLA, using a top-hat median gridding algorithm with a top-hat radius of  $6'$  (Barnes et al. 2001). The resulting pixel and beam sizes are  $4' \times 4'$  and  $15'.5$ , respectively. Spectral ringing associated with Galactic HI emission and the baseline ripple associated with strong continuum emission were respectively removed or suppressed using Hanning smoothing and the 'scaled template method' (see Barnes et al. 2001). Hanning smoothing increases the velocity resolution to  $27 \text{ km s}^{-1}$ .

Several sources of extraneous signal remained after standard processing. Residual baseline ripples caused by continuum radio sources are the most prominent. Hydrogen recombination lines at 1424.734 MHz (H166 $\alpha$ ), 1399.368 MHz (H167 $\alpha$ ), and 1374.601 MHz (H168 $\alpha$ ) appear at velocities of  $cz = -911 \text{ km s}^{-1}$ ,  $4507 \text{ km s}^{-1}$ , and  $9990 \text{ km s}^{-1}$ , respectively. Interference from the L3 beacon of the GPS near 1380 MHz ( $8778 \text{ km s}^{-1}$ ) is also present. These sources of interference can generally be identified by their characteristic frequencies and widths. In the case of recombination lines, they are accompanied by continuum emission from their underlying HII regions.

## 3. GALAXY SEARCH

The four Hanning-smoothed data cubes were visualized using KVIEW in the software package KARMA (Gooch 1995) and were searched by eye; the strong residual baseline ripples prevented the use of automatic galaxy-finding software. The galaxy search was conducted over the full velocity range,  $-1200 < cz < 12700 \text{ km s}^{-1}$ , although confusion from Galactic emission prevented a complete survey of the region with  $|v| < 250 \text{ km s}^{-1}$ . All possible planes, RA-Dec, RA-velocity, and Dec-velocity were examined by three independent parties and a final galaxy list was decided upon by a fourth author.

### 3.1. Determination of HI Properties

The coordinates and spectral characteristics of each galaxy were measured using the program MBSPECT in the software package MIRIAD (Sault, Teuben, & Wright 1995). The galaxy positions were determined by spatially fitting a Gaussian to the velocity-integrated emission of each galaxy. We subsequently used this position in the spectral analysis, where the weighted sum of the emission in each velocity plane was used to form the spectral profile. The total flux was measured by integrating the flux over the galaxy profile. The systemic velocity was taken to be the midpoint of the profile at 50% of the peak flux. The widths at 20% and 50% of the peak flux density were measured using a width-maximizing technique. Due to the large Hanning-smoothed velocity resolution of  $27 \text{ km s}^{-1}$ , the velocity widths we measure are broader than the intrinsic widths of the galaxies. The velocity widths at the 20% and 50% peak flux levels were therefore corrected by 21 and  $14 \text{ km s}^{-1}$ , respectively (see Henning et al. 2000). If the HI emission showed no evidence of extension or confusion, we analyzed a region  $28'$  around the galaxy. For seven of the galaxies, a narrower box of width  $12'$  or  $20'$  was used to isolate the galaxy emission from that arising from a neighboring galaxy, which may have led to an underestimation of the total flux. While no galaxies in our survey are clearly extended, we

<sup>6</sup> The Parkes telescope is part of the Australia Telescope which is funded by the Commonwealth of Australia for operation as a National Facility managed by CSIRO.

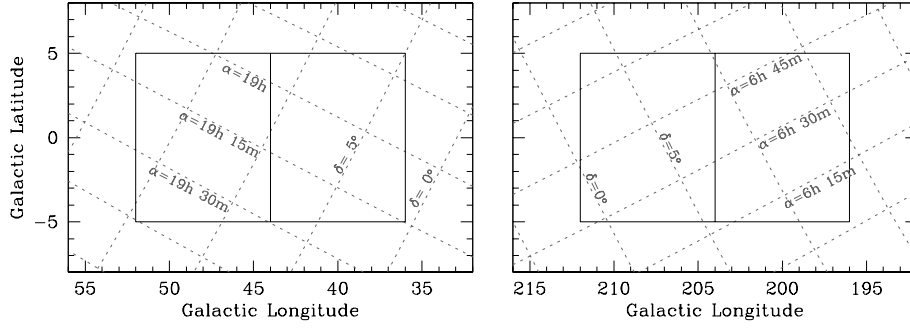


FIG. 1.— The survey region consists of four fields, each approximately  $8^\circ \times 10^\circ$ .

did identify one galaxy that is possibly extended or confused, J1912+02. The spectral fitting for this galaxy was conducted by summing the emission over a  $36' \times 36'$  box. The position was fit over a smaller  $12' \times 12'$  box.

Where possible, a first-order baseline was fit to each profile. For approximately half of the galaxies, however, baseline ripples made a first-order fit unrealistic; for these galaxies, we used the lowest order baseline that gave a reasonable fit. The distance to each galaxy,  $D = v_{LG}/H_0$ , was calculated using its velocity in the Local Group standard of rest,  $v_{LG} = v_{hel} + 300 \sin l \cos b$ . The HI mass was determined using  $M_{HI}[M_\odot] = 2.36 \times 10^5 D^2 F_{HI}$ , where  $D$  is the distance in Mpc and  $F_{HI}$  is the integrated HI flux in  $\text{Jy km s}^{-1}$ .

To estimate the errors on the HI parameters, we conducted a set of simulations. Each galaxy profile was first smoothed using a Savitzky-Golay smoothing filter (Press et al. 1992, Sec. 14.8). This least-squares polynomial filter reduces noise while better retaining the higher-order characteristics of the spectrum than traditional smoothing techniques. Fifty simulated spectra were then created for each galaxy by adding random Poisson noise to the smoothed galaxy spectrum; the rms of this random noise was set equal to that of the original galaxy spectrum. The errors on the HI parameters were then taken to be the median absolute offsets between the parameters of the 50 simulated spectra, as measured by MBSPECT, and those of the smoothed galaxy profile. The median errors on the peak and integrated flux for the entire sample of galaxies are approximately 9% and 4%, respectively. The median error on the systemic velocity is  $3 \text{ km s}^{-1}$  and the median errors on the 50% and 20% velocity widths are  $8 \text{ km s}^{-1}$  and  $10 \text{ km s}^{-1}$ , respectively. We note that the error we quote for the integrated flux does not take into account the uncertainty due to baseline subtraction or the uncertainty in calibration; the total errors on the integrated flux are likely to be  $\sim 10\text{--}15\%$ . We further discuss this method and the dependence of the estimated errors on S/N in Appendix A.

### 3.2. Results

77 definite or probable galaxies were detected, 35 in the  $l = 36^\circ$  to  $52^\circ$  region and 42 in the  $l = 196^\circ$  to  $212^\circ$  region. Because adjacent data cubes extend slightly beyond the  $8^\circ \times 10^\circ$  boundaries and overlap in Galactic longitude, 5 galaxies were initially detected twice. Of these, the detection located within the well defined  $8^\circ \times 10^\circ$  region of a cube was chosen for the final list. The HI properties of the 77 galaxies are presented in Table 1. The HI spectra of a subset of the sample

are shown in Figure 2; the complete set of spectra is available in the electronic edition of the Journal. The set of dotted lines nearest the galaxy spectrum defines the region in which the galaxy profile was measured. A second set of more widely spaced dotted lines indicate the region over which the baseline was fit. If no second set is present, the baseline fit was applied to the entire region displayed. All velocities are given in the optical convention,  $v = cz$ .

For several galaxies, a highly variable baseline prevents a convincing spectrum from being attained although the galaxy is clearly present in the data cube. As an example, consider J0623+14, a galaxy that was detected despite its superposition on one of the most extreme ripples that remain in the survey data. Coincidentally, J0623+14 has previously been observed by Arecibo in an HI follow-up survey of Weinberger galaxies (Pantoja et al. 1994). Despite the extremely poor baseline we observe, our HI parameters are in satisfactory agreement with the Arecibo HI parameters. The Arecibo flux is higher than what we detect by 14% and the peak flux density is lower by 22%. The most significant difference between our HI properties and those derived from the Arecibo observation is the 50% velocity width; we measure a value of  $286 \text{ km s}^{-1}$  whereas Pantoja et al. measure  $411 \text{ km s}^{-1}$ .

The identification of confused and marginally extended galaxies in our sample is difficult. We expect most normal galaxies to be unresolved in the Parkes beam at the typical distances in this survey, although confusion in the Parkes beam is not unlikely. The HI profile is the best indicator of a confused signal, although a profile can be intrinsically asymmetric, and minor contributions to the HI profile often do not disturb the profile greatly. A possible confusion in the detection can be confirmed by the relative positions and distances of the potential optical and IR counterparts, although background galaxies and HI-poor counterparts make this difficult, as does the high extinction in the ZOA. The unambiguous identification of confused galaxies can therefore only be made by high-resolution follow-up observations.

The mass distribution of the survey galaxies is shown in Figure 3. The HI masses range from  $1.0 \times 10^7 M_\odot$  to  $3.6 \times 10^{10} M_\odot$ , with a mean mass of  $4.3 \times 10^9 M_\odot$ . The distributions of velocities in the Local Group (solid line) and heliocentric (dotted line) standards of rest are shown in Figure 4. By using the Local Group standard of rest, we remove the effect of the Milky Way's velocity within the Local Group from our velocity and distance determinations. As we are in-

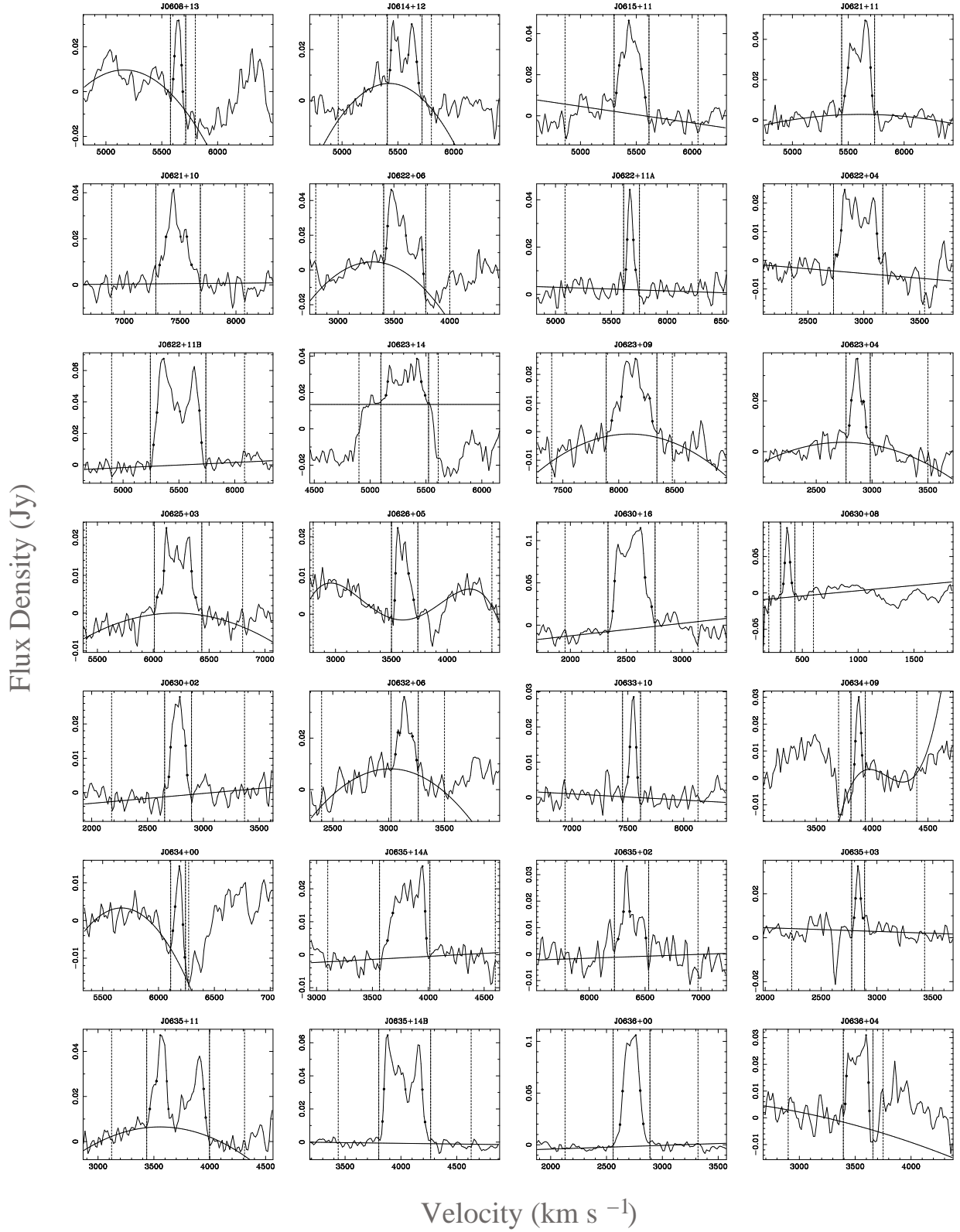


FIG. 2.— HI spectra of a subset of the survey galaxies. The spectra of all 77 galaxies are available in the electronic edition of the Journal. The inner dotted lines indicate the range in velocity over which the galaxy profile was measured. The outer dotted lines indicate the region over which the baseline was fit.

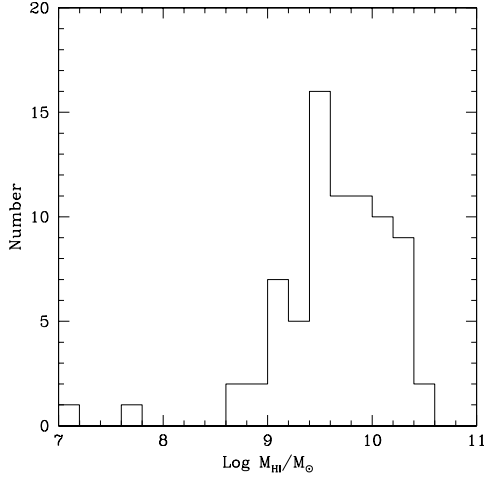


FIG. 3.— Mass distribution of galaxies detected in the survey. The mean mass is  $4.3 \times 10^9 M_\odot$ .

interested in large-scale structures outside of the Local Group, we feel that this is the more appropriate standard of rest. Both the velocities in the Local Group and heliocentric standards of rest have been plotted in Figure 4, however, for comparison. Distinct peaks can be seen at Local Group standard of rest velocities near  $3250 \text{ km s}^{-1}$ ,  $4750 \text{ km s}^{-1}$ , and  $6750 \text{ km s}^{-1}$  in the  $l = 36^\circ$  to  $52^\circ$  region which seem to be due to filaments crossing the Galactic plane at those velocities (see also Fig. 10). The first of these peaks seems to be due to the boundary of the Local Void. The velocity distribution for the  $l = 196^\circ$  to  $212^\circ$  region seems smoother overall, except for the curious gap around  $4500 \text{ km s}^{-1}$ . As will be discussed in §5, this structure may be due to the wall of the Canis Major Void.

### 3.3. Nearby Galaxies

Of the 77 galaxies detected in this survey, three have systemic velocities of  $cz < 700 \text{ km s}^{-1}$ . The newly detected galaxy HIZOA J0630+08 ( $l, b = 203.1^\circ, -0.9^\circ$ ) has a velocity of only  $367 \pm 1 \text{ km s}^{-1}$  (see Table 1) and could be a high velocity cloud, though its isolation and relative compactness suggest it is more likely a nearby dwarf galaxy. The Galactic extinction towards this galaxy is  $A_B \sim 3 \text{ mag}$  (Schlegel et al. 1998). HIZOA J0630+08 may be part of the Orion Group (Giovanelli & Haynes 1981) whose known members are the Orion Dwarf ( $l, b = 200.6^\circ, -12.3^\circ$ ), the irregular galaxy 0554+07 ( $l, b = 200.0^\circ, -8.4^\circ$ ), the dwarf irregular galaxy CGCG 422-003 ( $l, b = 198.8^\circ, -12.2^\circ$ ) and UGC 03303 ( $l, b = 198.6^\circ, -16.9^\circ$ ). Their velocities are  $cz = 365, 411, 441$  and  $521 \text{ km s}^{-1}$ , respectively (Giovanelli 1979, Giovanelli & Haynes 1981, Michel & Huchra 1988, Thuan & Seitzer 1979). Karachentsev & Musella (1996) give distances of  $6.4 \pm 2.2 \text{ Mpc}$  (Orion Dwarf) and  $5.5 \pm 1.9 \text{ Mpc}$  (0554+07) assuming Galactic extinctions of 2.7 and 2.9 mag, respectively. At a distance of 6 Mpc the HI mass of HIZOA J0630+08 would be  $4 \times 10^7 M_\odot$ . Further investigations of the Orion Group and surroundings are under way.

In addition to HIZOA J0630+08, we detect two other nearby galaxies, HIZOA J1940+11 and HIZOA J1914+10, with systemic velocities of  $580 \text{ km s}^{-1}$  and  $654 \text{ km s}^{-1}$ , respectively. For HIZOA J1914+10 we derive an HI mass of  $M_{\text{HI}} = 6.5 \times 10^8 M_\odot$ . This galaxy was previously detected in the Dwingeloo Obscured Galaxies Survey and is known as

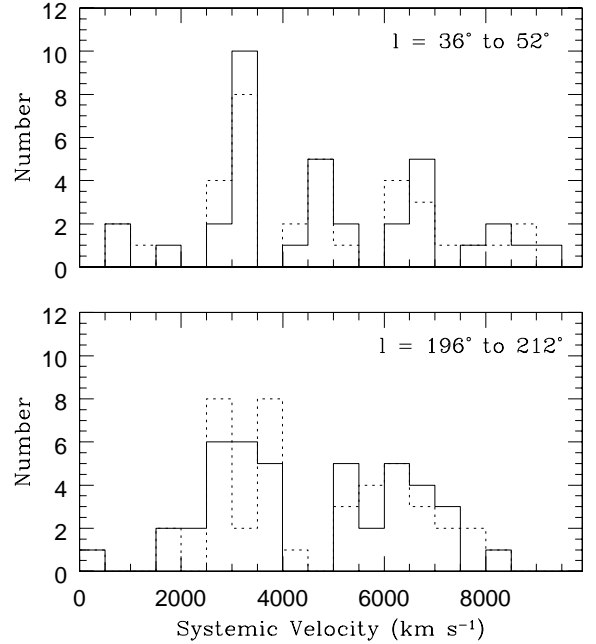


FIG. 4.— Velocity distribution for galaxies in the  $l = 36^\circ$  to  $52^\circ$  and  $l = 196^\circ$  to  $212^\circ$  regions. The velocity distributions in the Local Group and heliocentric standards of rest are given by a solid line and a dotted line, respectively.

Dw044.8-0.5 (Henning et al. 1998, Rivers 2000). The Galactic extinction in this direction is extremely high, preventing detection of optical or infrared counterparts.

For HIZOA J1940+11, a newly cataloged galaxy, we derive an HI mass of only  $M_{\text{HI}} = 4.1 \times 10^7 M_\odot$ . Confirmation of this HI detection would be desirable as it is very weak and found at the edge of our survey field. The Galactic extinction in this direction is  $A_B \sim 2 \text{ mag}$  (Schlegel et al. 1998). Both HIZOA J1940+11 and HIZOA J1914+10 appear isolated, in contrast to HIZOA J0630+08, and lie in the outskirts of the Local Void.

### 3.4. Survey Completeness

Our ability to detect a galaxy in the survey depends on both its integrated flux and velocity width. A galaxy with a high total flux and a small to moderate velocity width can be identified most easily; decreasing a galaxy's flux or increasing its velocity width would generally make detection more difficult. This, and previous experience with HI surveys (e.g. Kilborn et al. 2002), leads us to expect the survey to be approximately mean flux limited, where mean flux is defined here to be the integrated flux divided by the 20% velocity width (or the 50% velocity width in cases where the 20% width is not available). This expectation is confirmed by plotting the number of survey galaxies with a given flux,  $N(S)$ , where  $S$  is defined to be the mean, integrated, or peak flux density. We find that  $N(S)$  declines most steeply at low fluxes, and therefore best defines the flux cutoff, when the flux is taken to be the mean flux density.

A plot of  $N(S)$  against  $S$  is shown in Fig. 5, with  $S$  representing the mean flux density as above. It is consistent with a Euclidean power law,  $N(S) \propto S_{\text{mean}}^{-2.5}$ , and a mean flux density

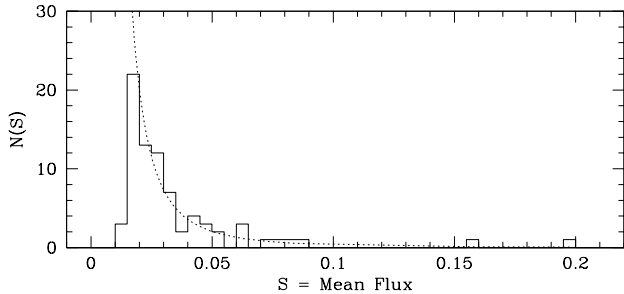


FIG. 5.— Number of survey galaxies with a given mean flux density. A Euclidean power law,  $N(S) \propto S_{\text{mean}}^{-2.5}$ , has been fit to the data. The approximate mean flux completeness limit, 0.022 Jy, was determined by averaging the fit of this power law to regions of low, medium, and high rms noise.

completeness limit of 0.022 Jy, assuming approximate spatial homogeneity. The best-fit linear relationship between the mean flux density and peak flux density of galaxies in the survey has a slope of 0.75. The above completeness limit therefore corresponds roughly to a peak flux density completeness limit of 0.029 Jy, which is  $\sim 5\sigma$  above the rms noise of the survey, 6.0 mJy.

In Figure 6, we plot as a solid histogram the area of the survey,  $A(\leq S)$ , at or below a given rms noise,  $S$ . The number of galaxies detected at or below a given rms noise is also given as a dotted histogram. We conservatively define the effective area of the survey to be the area with an rms noise at or below 0.0073 Jy, 239  $\text{deg}^2$ . Inside this area, the limiting mean flux density of the survey, 0.022 Jy, corresponds to a  $3\sigma$ , or higher, detection (corresponding to  $5\sigma$ , or higher, in peak flux density). This area is less than the nominal survey area of  $4 \times 8^\circ \times 10^\circ = 320 \text{ deg}^2$  partly because of edge effects, and partly because of the increased continuum (particularly residual continuum ripple) along the Galactic Plane.

To investigate the effect of the variable rms, we divide the survey into three regions of equal area, but of different rms noise. We again plot  $N(S)$  against  $S$  for each of the three regions and fit the differential number counts with a Euclidean power law. We estimate completeness limits of 0.019, 0.020 and 0.026 Jy for the regions of low, medium, and high rms noise, respectively. As expected, the completeness limit increases with rms noise. However, the variation is sufficiently limited that, for the present purposes, a mean completeness limit of 0.022 Jy adequately characterizes the survey.

Finally, it is worth noting that, in addition to good completeness above a mean flux density of 0.022 Jy, this survey is expected to be highly reliable. Galaxy identifications were made by three authors independently, and the final galaxy list was made by a fourth author in a conservative manner, guided by experience gained from follow-up observations of surveys with similar noise characteristics (Henning et al. 2000, Zwaan et al. 2004). We expect that very few, if any, of the new galaxies presented here will be false detections, and therefore the reliability of the catalog to be close to 100%. Ultimately, however, follow-up HI observations of some weaker objects will be required to ensure that no false detections remain.

#### 4. MULTIWAVELENGTH COUNTERPARTS

The region of sky covered by the northern ZOA survey overlaps slightly with a number of other surveys. These include four blind HI surveys, the Arecibo Dual Beam Sur-

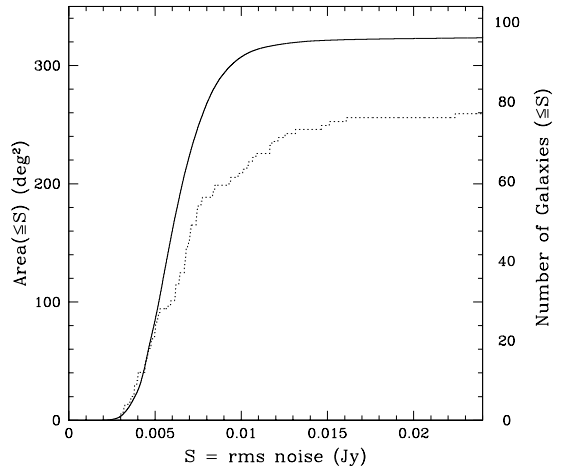


FIG. 6.— Histogram of the survey area (solid line, left axis) and number of galaxies (dotted line, right axis) detected at or below a given rms noise. The survey completeness is set to be the area of the survey with an rms noise at or below 0.0073 Jy.

vey (ADBS; Rosenberg & Schneider 2000), the pilot NRAO 300-ft telescope survey (Henning 1992), the Dwingeloo Obscured Galaxy Survey (DOGS; Henning et al. 1998, Rivers 2000), and the HI Parkes Zone of Avoidance Shallow Survey (HIZSS; Henning et al. 2000), although the overlap with the HIZSS is extremely small. This region also coincides with a number of HI follow-up surveys and several optical surveys, from which the ZOAG (see Lercher, Kerber, & Weinberger 1996), CGMW (see Roman, Iwata, & Saito 2000), WEIN (Weinberger 1980), and additional catalogs have been compiled. Significant infrared coverage of these regions has been provided by IRAS and 2MASS.

#### 4.1. Counterpart Search

We searched for HI, optical, and infrared counterparts to the northern ZOA galaxies using two methods. We first used the NASA/IPAC Extragalactic Database (NED<sup>7</sup>), the 2MASS Extended Source Catalog (XSC<sup>8</sup>), and the IRAS Point Source Catalog (PSC) to conduct an automated search for the *nearest* potential counterparts to each HI galaxy. The fraction of these counterparts likely to be associated with the HI galaxies was estimated by a simulation, described in Appendix B. Our second approach was to determine the most likely counterparts by searching for and visually inspecting all potential optical and infrared counterparts, including (1) counterparts located further from the HI position than those chosen by our previous search and (2) previously unidentified galaxies in the Digitized Sky Survey (DSS<sup>9</sup>) POSS-II near-infrared, red, and

<sup>7</sup> This research has made use of the NASA/IPAC Extragalactic Database (NED) which is operated by the Jet Propulsion Laboratory, California Institute of Technology, under contract with the National Aeronautics and Space Administration.

<sup>8</sup> This publication makes use of data products from the Two Micron All Sky Survey, which is a joint project of the University of Massachusetts and the Infrared Processing and Analysis Center/California Institute of Technology, funded by the National Aeronautics and Space Administration and the National Science Foundation.

<sup>9</sup> The Digitized Sky Surveys were produced at the Space Telescope Science Institute under U.S. Government grant NAG W-2166. The images of

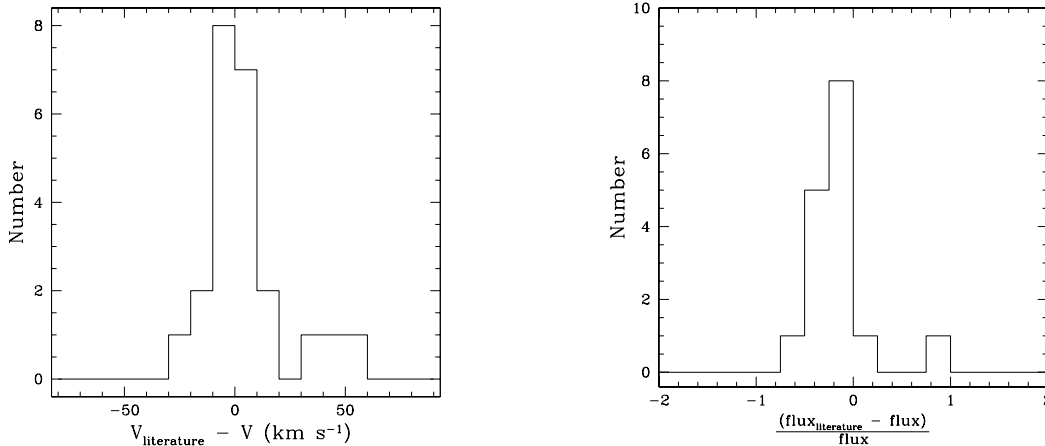


FIG. 7.— Histograms of the offset between the HI velocities and fluxes measured by our survey, and those from the literature. The mean offset in velocity is  $6 \text{ km s}^{-1}$  and that in flux is  $-16\%$ .

blue images. Any galaxy visible in the DSS bands was classified by us as an optical detection. The visual search is, of course, subject to error; we have tried to minimize this error by having multiple authors participate in the choice of counterparts. Previous investigations of the offset between Parkes HI sources and their counterparts (see Juraszek et al. 2000, Koribalski et al. 2004, Ryan-Weber et al. 2002) indicate that while most counterparts are found within  $3'$ , offsets as high as  $5'$  are not highly unusual. A conservative search radius of  $10'$  was used for the initial searches to ensure that no potential counterparts were missed.

#### 4.2. Previously Detected HI Galaxies

Of the 77 galaxies detected here, 20 have been detected previously in HI. We have detected all galaxies from the ADBS, NRAO 300-ft, HIZSS, and DOGS blind HI surveys that lie in our survey region, although J0635+11 was resolved into two galaxies separated by  $4'$  by the ADBS. We have also detected several galaxies from follow-up HI surveys. Figure 7 illustrates the difference between our measured systemic HI velocities and the HI velocities given by NED as well as the fractional differences in flux between our survey and measurements in the literature (Rosenberg & Schneider 2000, Pantoja et al. 1997, Pantoja et al. 1994, Theureau et al. 1998, Henning et al. 2000, Rivers 2000). The distribution of velocity offsets has a mean of  $6 \text{ km s}^{-1}$  and a dispersion of  $19 \text{ km s}^{-1}$ . The flux we measure is offset by an average of  $-16\%$  from the values in the literature, with a dispersion of  $32\%$ .

The galaxies with the largest positive and negative flux offsets are HIZOA J0654+08 and HIZOA J0622+11B, respectively. Both were previously observed as part of the Arecibo Dual Beam Survey. The small ADBS flux for HIZOA J0622+11B can potentially be explained by the fact that ADBS flux measurements were underestimated if the source was offset from the beam center (see Rosenberg and Schneider 2000). We are confident in our fits to both galaxies, and are unable to explain the large positive flux offset of HIZOA J0654+08.

Two of the remaining galaxies for which our flux is sig-

nificantly higher than that in the literature were identified by the Dwingeloo Obscured Galaxies Survey. Both have strong clean profiles. The discrepancies in flux most likely arise from the conservative way in which the Dwingeloo galaxy fluxes were measured (Rivers (2000) defined the total integrated flux to be the flux inside the  $N_{\text{HI}} = 1.25 \times 10^{20} \text{ cm}^{-2}$  contour). Also, as the Dwingeloo fluxes were measured from VLA maps, any extended emission would have been missed by the interferometer.

#### 4.3. Results of Counterpart Search

We present in Table 2 the HI counterparts from other surveys of the ZOA galaxies, along with the most likely optical, 2MASS, and IRAS counterparts. For the latter group, we include only those sources that were visually verified to be likely counterparts. Potential counterparts were discarded from this list if they did not appear to be a galaxy, were offset from the HI position by a statistically unlikely amount ( $\gtrsim 4'$ ), or were of an unlikely galaxy type. In seven cases, the 2MASS counterpart that was chosen by the visual inspection was not the counterpart closest to the HI position. All likely optical and IRAS counterparts (excluding the DSS galaxies which were not found via the automated NED search) were the counterparts nearest the HI position. In Table 3, we give the positions of the newly detected DSS counterparts.

The spatial distribution of sources with multiwavelength counterparts is shown in Figure 8, where solid circles represent galaxies with both optical and infrared counterparts, solid triangles represent galaxies with optical counterparts only, and solid stars represent galaxies with infrared counterparts only. HI galaxies with no counterparts are given as crossed open circles. We have overlaid contours of  $E(B-V)$  on Figure 8 using the DIRBE/IRAS data. Contour values of  $1^{\text{m}}.0$  and  $3^{\text{m}}.0$  were used for the  $l = 36^\circ$  to  $52^\circ$  region, whereas values of  $0^{\text{m}}.3$  and  $0^{\text{m}}.8$  were used for the contours of the  $l = 196^\circ$  to  $212^\circ$  region.

In summary, 19 of our 77 galaxies have likely optical counterparts, 27 have likely 2MASS counterparts, and 11 have likely IRAS counterparts. In addition, 16 galaxies have likely optical DSS counterparts that are previously uncatalogued. The percentage of counterparts found via the automated search that were still considered likely after a visual verification is roughly consistent with the expected percent-

these surveys are based on photographic data obtained using the Oschin Schmidt Telescope on Palomar Mountain and the UK Schmidt Telescope. The plates were processed into the present compressed digital form with the permission of these institutions.

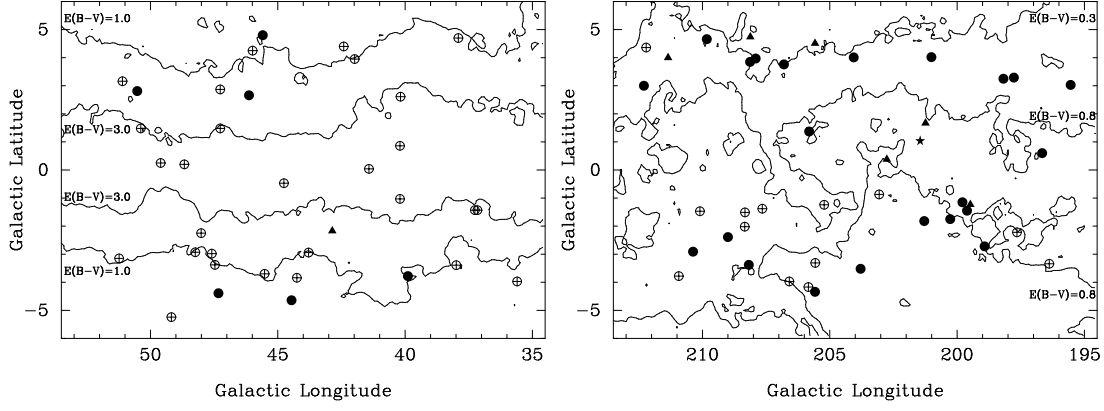


FIG. 8.— Spatial distribution of galaxies. HI galaxies with no counterparts are represented by crossed open circles. Solid circles represent galaxies with both optical and infrared counterparts, solid triangles represent galaxies with optical counterparts only, and solid stars represent galaxies with infrared counterparts only. The counterparts used in this plot are only those that remain after the visual verification. The contours overlaid on the plot are contours of  $E(B-V)$  (Schlegel et al. 1998), with values of  $1^m.0$  and  $3^m.0$  for the  $l = 36^\circ$  to  $52^\circ$  region, and  $0^m.3$  and  $0^m.8$  for the  $l = 196^\circ$  to  $212^\circ$  region.

ages calculated by means of the simulations discussed in Appendix B.

#### 5. LARGE-SCALE STRUCTURE

The spatial distribution of galaxies in our survey can be found in Figures 9 through 12. In Figures 9 and 11, the HI galaxies detected in our survey are given by solid points. We have plotted as open points all galaxies in the Lyon-Meudon Extragalactic Database (LEDAs)<sup>10</sup> with known velocities. In each velocity-slice, the galaxies with the lowest velocities are represented by triangles; medium and high velocity galaxies are plotted as squares and circles, respectively. The dotted box outlines the region sampled by our survey. In the cone diagrams of Figures 10 and 12, the HI galaxies are plotted as solid circles and LEDA galaxies are plotted as open circles. The survey region is again defined by dotted lines. The velocities in Figures 9, 10, 11, and 12 have been converted to the Local Group standard of rest. Void parameters are taken from Fairall (1998) and are given in Table 4.

The  $l = 36^\circ$  to  $52^\circ$  region lies near several voids, including the Local, Microscopium, and Cygnus Voids. At first glance it appears that the galaxies detected in our survey may define the edge of the Local and/or Microscopium Voids, but we caution that preliminary results from the full ZOA survey indicate that the number of galaxies rises slightly as one moves from our survey region towards the Local and Microscopium Voids before dropping off at Galactic longitudes of  $10^\circ < l < 20^\circ$ .

When visualized including even larger areas (not shown here), the nearby detected galaxies that produce the distinct peak around  $3000 \text{ km s}^{-1}$  appear to be the smooth continuation of the sine-wave like feature that can be traced across the whole southern sky (Kraan-Korteweg, Koribalski, & Juraszek 1999). This wave feature crosses the Milky Way in Puppis and continues towards the Antlia, Hydra, and Centaurus structures before folding back across the Galactic Plane in a structure called the Centaurus Wall by Fairall (1998). This wave encircles the Local Void while crossing the ZOA for a third time towards the region inspected here.

The second peak in the velocity distribution around

<sup>10</sup> <http://leda.univ-lyon1.fr> – the Lyon-Meudon Extragalactic Database is supplied by the LEDA team at the Centre de Recherche Astronomique de Lyon.

TABLE 3  
NEW DSS COUNTERPARTS

HIZOA	$\alpha_{2000}$	$\delta_{2000}$
J0622+11A	06 21 59.4	+11 18 38
J0634+09	06 34 04.9	+09 12 55
J0635+11	06 35 54.6	+11 08 10
J0641+01 <sup>a</sup>	06 41 04.4	+01 50 24
J0659+06	06 59 38.1	+06 27 19
J0702+03	07 02 50.4	+03 11 14
J1853+09 <sup>a</sup>	18 53 47.5	+09 51 16
J1917+07	19 17 24.8	+07 49 07
J1927+09 <sup>a</sup>	19 27 49.5	+09 27 32
J1929+08	19 29 19.9	+08 02 42
J1930+12 <sup>a</sup>	19 30 32.2	+12 11 41

<sup>a</sup>We see a galaxy at this position, but cannot determine whether it is the correct counterpart to the HI galaxy.

TABLE 4  
VOID PARAMETERS FROM FAIRALL (1998)

Name	$l$ (deg)	$b$ (deg)	$cz$ ( $\text{km s}^{-1}$ )	radius ( $\text{km s}^{-1}$ )
Aquarius Void	60	-41	4500	1500
Canis Major Void	229	-13	5000	2500
Capricornus Void	2	-17	8500	$\sim 2500$
Cor Bor Void	58	37	5200	2000
Cygnus Void	67	-9	3500	1250
Delphinus Void	59	-6	2500	1500
Gemini Void	172	9	3000	$\sim 1250$
Local Void	18	6	1500	1500
Microscopium Void	10	1	4500	1750
Orion Void	206	-2	1500	750
Taurus Void	167	-29	4000	$\sim 2000$

$4500 \text{ km s}^{-1}$  also seems to be due to a clear filament present in both the middle panel of Figure 9 as well as the redshift cones of Figure 10. Here, the detected galaxies seem to divide the Microscopium and Cygnus/Delphinus Voids, the lat-



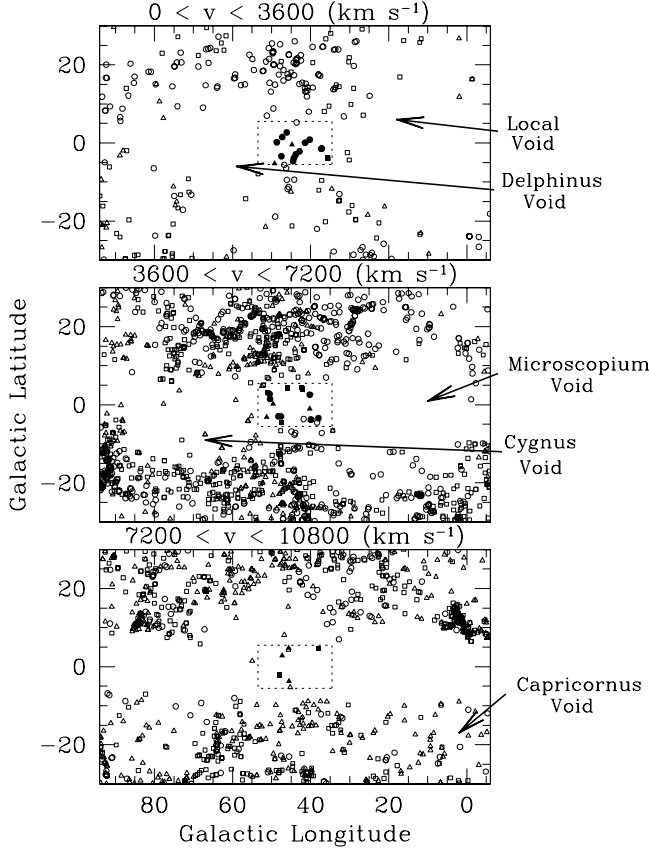


FIG. 9.— Spatial distribution of galaxies in the  $l = 36^\circ$  to  $52^\circ$  region. The velocities are in the Local Group standard of rest. The dotted line outlines the survey region. HI galaxies detected by this survey are represented by solid points; LEDA galaxies are given by open points. In each velocity range, triangles, squares, and circles represent the galaxies in the low, middle, and high velocity bins, respectively. The dotted line outlines the survey region.

ter two of which are likely to form one void rather than two distinct voids.

There are several large-scale structures in the vicinity of the  $l = 196^\circ$  to  $212^\circ$  region, which lies between the Perseus-Pisces supercluster and the Puppis filament. Two of the nearest newly-detected galaxies, HIZOA J0700+01 and HIZOA J0705+02, are found within 4.8 and 4.9 Mpc of the center of the Orion Void. This void ( $l, b, cz = 206^\circ, -2.0^\circ, 1500 \text{ km s}^{-1}$ ) was previously thought to have a radius of  $750 \text{ km s}^{-1}$ , or 10 Mpc (Fairall 1998). The LEDA Database, however, contains 42 galaxies that lie between 5 Mpc and 10 Mpc of the void center, and two that lie at smaller radii (4.6 and 4.9 Mpc). It therefore appears that the true radius of this void is approximately 5.0 Mpc and that the two galaxies detected here lie along its edge.

The galaxies between  $2500$  and  $5500 \text{ km s}^{-1}$  seem to provide the border of two voids, the Gemini Void, now quite prominent in the upper panel of Figure 11, and the Canis Major Void, which now seems slightly smaller and centered at higher latitudes ( $l, b, cz = 220^\circ, 0^\circ, 5000 \text{ km s}^{-1}$ ) as compared to its location as given by Fairall 1998 ( $l, b, cz = 229^\circ, -13^\circ, 5000 \text{ km s}^{-1}$ ). The distinct gap between  $4000$  and  $5000 \text{ km s}^{-1}$  in the velocity distribution (Fig. 4) is due to the fact that the continuous part of the border of the Canis Major

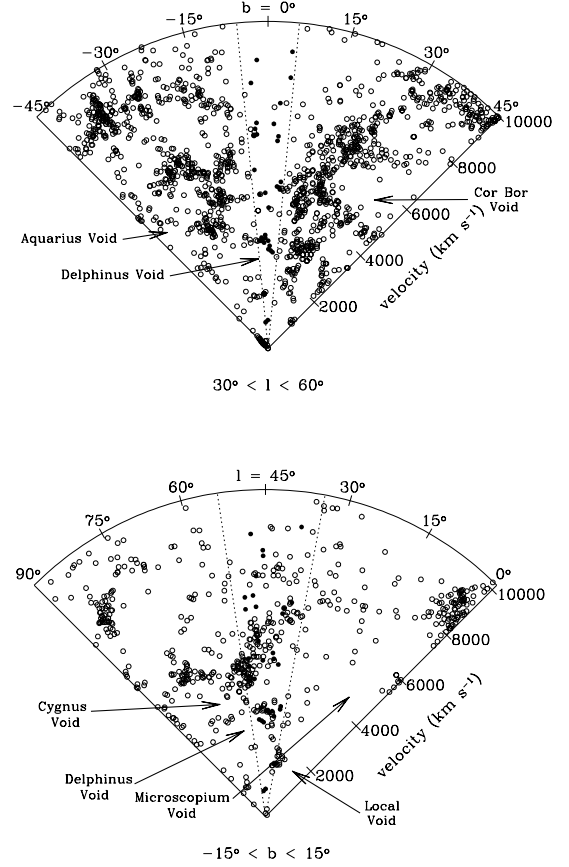


FIG. 10.— Cone diagrams of galaxies in the  $l = 36^\circ$  to  $52^\circ$  region. The velocities are in the Local Group standard of rest. HI galaxies detected by this survey are represented by solid circles; LEDA galaxies are given by open circles. The survey region is defined by dotted lines.

Void between  $4000$  and  $5000 \text{ km s}^{-1}$  falls just outside of our survey regions and crosses the ZOA at quite constant velocities.

## 6. MASS FUNCTION

Over the past several years, a number of attempts have been made to better define the HI mass function. Most recently, the HIPASS Bright Galaxy Catalog (BGC, Zwaan et al. 2003) and the ADBS (Rosenberg & Schneider 2002) have been utilized. Prior to these surveys, which cataloged 1000 and 265 galaxies, respectively, the HIPASS SCC (Kilborn 2000), the HIPASS HIZSS (Henning et al. 2000), and the AHIS (Zwaan et al. 1997) provided the best estimates to the mass function. The sensitivity and coverage of our survey do not allow us to estimate the mass function any more precisely than these recent measurements, especially at the low-mass end where the slope of the mass function is most uncertain. Determining the mass function is still of interest, however, as it allows an investigation of the comparative mass density and distribution of galaxies in our survey region, as well as a rough comparison with previous estimations.

We calculate the HI mass function in two ways, the standard  $1/V_{\text{max}}$  method (Schmidt 1968) and a refined  $1/V_{\text{max}}$  method (Saunders et al. 1990). The latter incorporates the density profile of the galaxies into the calculation to reduce

TABLE 5  
SCHECHTER PARAMETERS

Method	$\log \Theta^*$	$\alpha$	$\log M_{\text{HI}}^*$	$\log \text{HI density}^a$	$\log \text{HI density}^b$
$1/V_{\text{max}}$	$-2.33 \pm 0.33$	$1.13 \pm 0.36$	$9.85 \pm 0.19$	$7.56 \pm 0.42$	$7.55^{+0.07}_{-0.08}$
Modified $1/V_{\text{max}}$	$-2.35 \pm 0.32$	$1.16 \pm 0.27$	$10.05 \pm 0.20$	$7.75 \pm 0.37$	...

<sup>a</sup>HI mass density calculated from Schechter parameters ( $\log M_{\odot} \text{ Mpc}^{-3}$ )

<sup>b</sup>HI mass density calculated from  $\Sigma \frac{M_{\text{HI}}}{V_{\text{max}}}$  ( $\log M_{\odot} \text{ Mpc}^{-3}$ )

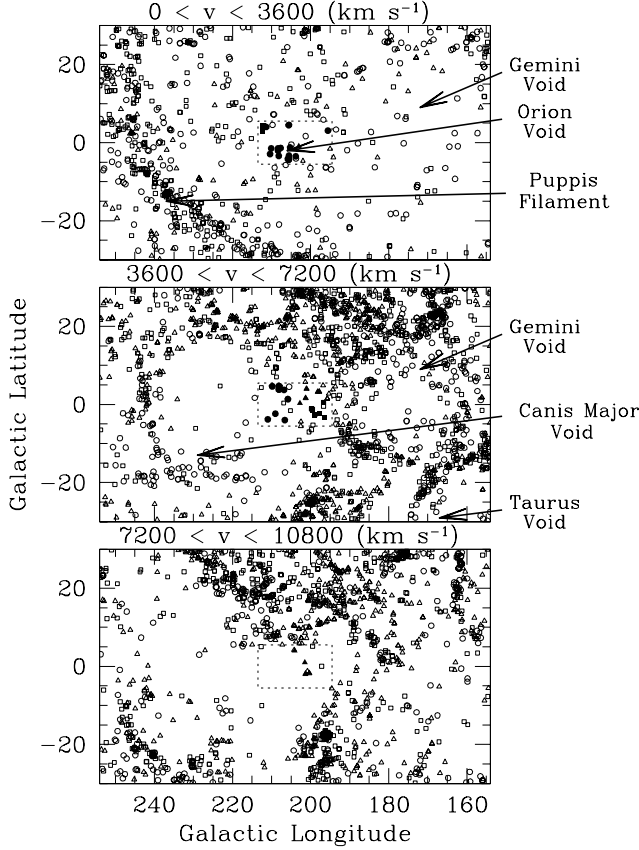


FIG. 11.— Spatial distribution of galaxies in the  $l = 196^\circ$  to  $212^\circ$  region. The velocities are in the Local Group standard of rest. The dotted line outlines the survey region. HI galaxies detected by this survey are represented by solid points; LEDA galaxies are given by open points. In each velocity range, triangles, squares, and circles represent the galaxies in the low, middle, and high velocity bins, respectively. The dotted line outlines the survey region.

the effect of clustering and large-scale structure. The standard  $1/V_{\text{max}}$  method non-parametrically determines the mass function by weighting each galaxy's mass by the inverse of the maximum volume in which it could be detected by the survey. This method, however, is potentially affected by large-scale structure, as it assumes that the galaxy population has a homogeneous distribution. The Saunders et al. method is able to remove the majority of the effects of large-scale structure by first using a maximum likelihood technique to determine the radial density distribution of the sample,  $p(r)$ . This density profile is used to define an effective volume,  $V_{\text{eff}} = \int_0^{r_{\text{max},i}} r^2 p(r) dr$ , which replaces  $V_{\text{max}}$  in the  $1/V_{\text{max}}$

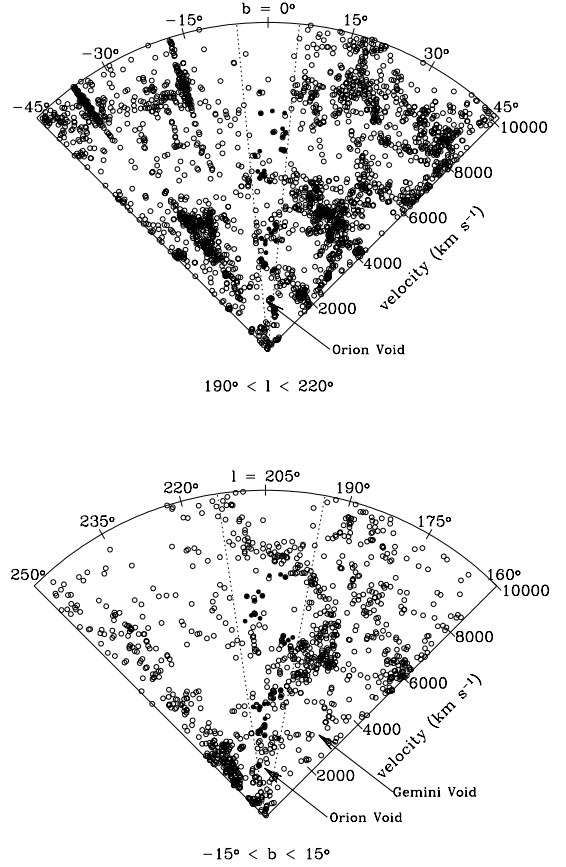


FIG. 12.— Cone diagrams of galaxies in the  $l = 196^\circ$  to  $212^\circ$  region. The velocities are in the Local Group standard of rest. HI galaxies detected by this survey are represented by solid circles; LEDA galaxies are given by open circles. The survey region is defined by dotted lines.

method. In both cases, the resulting mass function can be fit by a Schechter (1976) function:

$$\theta(M_{\text{HI}})dM_{\text{HI}} = \theta^* \left( \frac{M_{\text{HI}}}{M_{\text{HI}}^*} \right)^\alpha \exp\left(-\frac{M_{\text{HI}}}{M_{\text{HI}}^*}\right) dM_{\text{HI}}$$

The HI mass function can be found in Figure 13, where the data points from the standard  $1/V_{\text{max}}$  method are given by circles and the fit by a solid line. The modified  $1/V_{\text{max}}$  method is represented by triangular points and a dashed line. For comparison, the HI mass function determined from the BGC has been included on the plot, as a dotted line. Only those galaxies with a mean flux above our completeness limit of 0.022 Jy were included in the mass function calculation. A bin size of

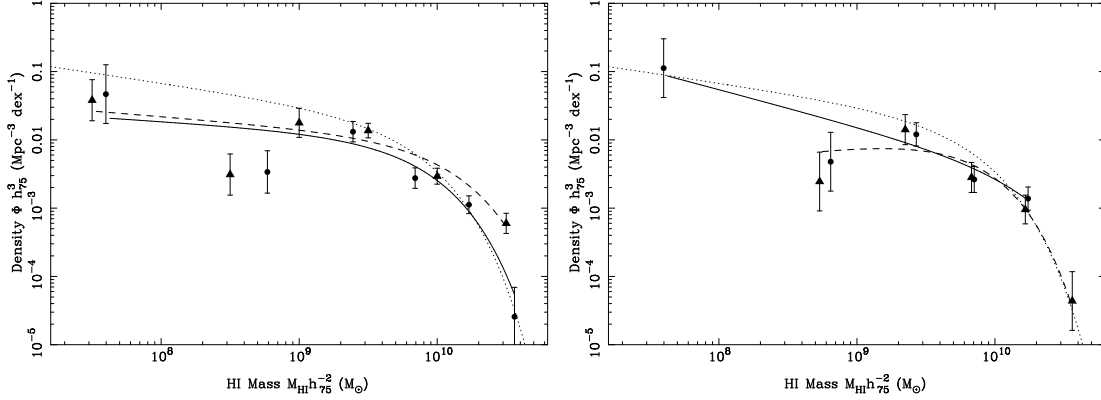


FIG. 13.— (a) HI mass function of the survey galaxies. The circles represent the mass function calculated from the standard  $1/V_{\text{max}}$  method. The solid line is a least-squares fit of a Schechter function for this method. The modified  $1/V_{\text{max}}$  method is represented by triangular points. The Schechter function fit for this method is given by a dashed line. (b) HI mass function of the two survey regions. The mass function of the  $l = 36^\circ$  to  $52^\circ$  region is represented by circular points and a solid line. The mass function of the  $l = 196^\circ$  to  $212^\circ$  region is represented by triangular points and a dashed line. The bin size is 0.5 dex; bins are plotted if one or more galaxies are present. Points are plotted at the mean mass within the bin for the standard method, and at the mean bin position for the modified method. For both plots, the dotted line represents the mass function from the HIPASS BGC (Zwaan et al. 2003).

0.5 dex was used for both techniques. For the standard  $1/V_{\text{max}}$  method, the points are plotted at the mean mass of the galaxies in each bin. Missing points indicate that we detect no galaxies in that bin. For the modified  $1/V_{\text{max}}$ , the points represent the middle of the mass bin. The galaxy J0635+11, which was resolved into two galaxies by the ADBS, does not affect our mass function, as its mean mass falls below our cutoff. For a discussion on the effects of confusion on HI mass functions, see Zwaan et al. (2003).

The Schechter parameters from the two methods as well as the derived HI mass densities can be found in Table 5. The two methods give similar mass functions, suggesting that large-scale structure in these regions does not strongly affect the calculation of the mass function. The largest deviation between the two methods occurs at the high-mass end, where the standard method is in better agreement with the BGC mass function than the modified method. In addition, the standard  $1/V_{\text{max}}$  method gives a  $\langle \frac{V}{V_{\text{max}}} \rangle$  of  $0.54 \pm 0.04$ , indicating that spatial inhomogeneity will not affect the results greatly. Both methods of estimating the mass function give a function that falls below that of the BGC at the low mass end, with the largest discrepancy coming from an underdensity of galaxies of mass  $M \sim 10^8 - 10^9 M_\odot$ . This offset may be due to an underdensity of mass in the regions examined. Zwaan et al. (2003) have shown that the four quadrants of the BGC give mass functions with similar values of  $M^*$  but with varying slopes and normalizations with a degree of variation similar to what we observe between our mass function and that derived from the BGC.

We also include in Figure 13 a plot of the mass functions for the two separate survey regions. The  $l = 36^\circ$  to  $52^\circ$  region is given by circular points and a solid line. The  $l = 196^\circ$  to  $212^\circ$  region is given by triangles and a dashed line. Due to the low number of galaxies, these mass functions are not highly reliable, but can still be used for general comparison purposes. The mass function for the  $l = 196^\circ$  to  $212^\circ$  region fits the BGC mass function remarkably well in the high-mass regime, whereas the  $l = 36^\circ$  to  $52^\circ$  region mass function provides the best fit to the BGC mass function in the low mass regime.

## 7. SUMMARY

We have detected 77 HI galaxies in the northern extension of the Parkes ZOA survey. The survey has a median rms noise of  $6.0 \text{ mJy beam}^{-1}$ , is approximately complete to a mean flux density of  $22 \text{ mJy}$ , and has an effective area of  $239 \text{ deg}^2$ . Of the 77 galaxies detected here, 19, 27, and 11 have likely optical, 2MASS, and IRAS counterparts already cataloged, respectively. In addition, a further 16 have likely optical counterparts visible in the Digitized Sky Survey. Twenty have been previously detected in HI. The spatial and velocity distributions of the galaxies in the  $l = 36^\circ$  to  $52^\circ$  region reveal several filaments that cross the Galactic plane, the nearest of which seems to be the continuation of a sine-wave like feature that can be traced across the whole southern sky. The medium-velocity galaxies in the  $l = 196^\circ$  to  $212^\circ$  region seem to provide the border of the Gemini and Canis Major Voids, whereas the detection of two new low-velocity galaxies within the Orion Void help to redefine its radius. Of particular interest is the galaxy HIZOA J0630+08 ( $l, b = 203^\circ, -0.9^\circ$ ), which has a velocity of  $367 \pm 1 \text{ km s}^{-1}$  in the heliocentric standard of rest. We suggest that it belongs to the nearby Orion Group which includes a small number of dwarf galaxies. An HI mass function was derived using both the standard  $1/V_{\text{max}}$  method and a revised  $1/V_{\text{max}}$  method that is less sensitive to large-scale structure. Both methods produce similar mass functions whose normalizations fall slightly below that of the HI Parkes Bright Galaxy Catalog. The observations for the southern Parkes ZOA survey are complete and analysis is currently underway. Upon completion, this survey will be combined with the northern extension studied here, which should considerably increase our understanding of the structure and dynamics of the obscured Local Universe.

We thank the staff of the Parkes radio telescope. Also Will Saunders for his implementation of the maximum likelihood  $1/V_{\text{max}}$  method. We gratefully acknowledge financial support from the Australian-American Fulbright Commission (JLD) and CONACYT research grant 40094-F (RCKK and JMII).

## APPENDIX

## A. ERRORS IN HI PROFILE PARAMETERS

To estimate the errors on the HI parameters, each galaxy profile was smoothed using a Savitzky-Golay smoothing filter with a smoothing width of 8 velocity channels (Press et al. 1992, Sec. 14.8). Fifty simulated spectra were then created for each galaxy by adding random Poisson noise to the smoothed galaxy spectrum; the rms of this random noise was set equal to that of the original galaxy spectrum. The errors on the HI parameters were then taken to be the median absolute offsets between the parameters of the 50 simulated spectra and those of the smoothed galaxy spectrum.

To better understand the errors on the HI parameters and the error simulation technique, we investigate below three additional aspects of the error estimation: (1) the effect of S/N on the measured errors, (2) the accuracy of the smoothing filter in preserving the galaxy parameters and (3) the biases introduced to the errors by the simulation process. We explore these issues using the spectrum of J1853+09, which has a S/N of 24. This spectrum, and the smoothed profile created using the Savitzky-Golay smoothing filter, are shown in Figure A1. A spectrum with a high S/N was chosen to ensure that the smoothed spectrum, used below as the template, was as representative as possible of a real galaxy profile.

To explore the effect of S/N on the errors, we began by running the error simulation, as described in §3.1, on the template. The simulation was run 21 times; on each occasion, the rms of the random Poisson noise was adjusted to give a desired S/N. The resulting set of 21 simulations have S/N ratios ranging incrementally from 3 to 24. The errors on the HI parameters, as a function of S/N, are given in Figure A2(a), where the points represent the median errors and the error bars represent the median absolute value of the errors (in both the +y and -y directions). The errors begin to rise at a S/N of 10, and do so quite substantially for S/N < 5. This result is in agreement with that of Roth, Mould, & Staveley-Smith (1994), who performed a similar set of simulations and found that the errors on HI line widths are particularly unreliable for S/N < 5. Of the 77 galaxies in our survey, none have a peak S/N < 5, 21 have 5 < S/N < 10, and 56 have S/N > 10.

Each of the 21 error simulations described above created 50 simulated galaxy profiles with a given S/N. To investigate the ability of the smoothing filter to preserve the galaxy profile, we next smoothed each set of 50 simulated profiles using the Savitzky-Golay smoothing filter. The HI parameters of the smoothed spectra were then measured by MBSPECT. Figure A2(b) illustrates the difference between the HI parameters of the spectra for which noise was added and then removed and the HI parameters of the original smoothed profile. There are several systematic offsets. For S/N ≥ 6, the peak flux density from the simulated profiles is lower than the peak flux density of the original smoothed profile, as expected from the smoothing process. This offset is quite low, however, tending towards 5% at high S/N. The total flux, systemic velocity, 50% velocity width, and 20% velocity widths are all slightly larger in the simulated smoothed profiles, but remain relatively constant down to S/N ratios of 5, below which the differences in peak flux density, total flux, and 20% velocity width increase. While it is not surprising that the smoothing filter increases the total flux and velocity widths, the increase in the systemic velocity is unexpected. This change, however, is due to the particular spectrum being used here, and will likely vary with different profiles. As can be seen in Figure A1, the overestimation of the velocity at the high-velocity end of the profile is larger than the underestimation at the low-velocity end, leading to a slight (~ 2 km s<sup>-1</sup>) overestimation of the systemic velocity.

We lastly investigate how the changes in smoothed parameters discussed above affect the error estimation. To do so, the error simulations were run on each of the 50 simulated galaxy profiles with a given S/N ratio. Recall that these 50 simulated spectra were created by adding random noise with a given rms to the template. By running the simulations on these 50 profiles, we remove the noise that we added (the step explored in the last paragraph) and then re-add it to the smoothed spectra. If no biases are introduced by the simulation process, the errors now measured should be equal to the errors estimated by running the simulations on the original spectrum of J1853+09. Figure A2(c) illustrates the differences between the errors derived from the simulated profiles and those estimated from the template. The largest bias introduced by the simulation process is the underestimation of the error on the 20% velocity width for spectra with low S/N ratios. At S/N ≥ 10, the error on the peak flux is overestimated by ~ 1.6% and the error on the total flux is underestimated by ~ 0.8%. The errors on the systemic velocity, 50% velocity width, and 20% velocity width are offset by an average of -0.2 km s<sup>-1</sup>, -0.9 km s<sup>-1</sup>, and 0.2 km s<sup>-1</sup>. At moderate to high S/N, these offsets are all well within the median errors measured for the galaxies in this sample (see §3.1), confirming the reliability of this process in estimating errors.

## B. COUNTERPART LIKELIHOOD SIMULATIONS

To investigate the likelihood that the *nearest* potential optical and infrared counterparts within both 3' and 5' of the HI position are real counterparts of the HI galaxies, a simulation was performed. In this simulation, fiducial HI detections were placed across our survey region. The positions of these simulated detections were defined by a grid of 120 positions at 20 arcminutes intervals surrounding each of the 77 galaxies. Using NED, the 2MASS XSC, and the IRAS PSC, counterparts of these false objects were searched for. By measuring the number of objects near these random positions, we determined the number of spurious counterparts expected for our real galaxies, and thus the probability,  $P$ , that the potential counterparts we detect are in fact related to the HI galaxies.

$$P = \frac{N_{\text{counterparts}} - N_{\text{unrelated}}}{N_{\text{counterparts}}} \quad (\text{B1})$$

$$N_{\text{unrelated}} = \frac{N_{\text{simulated galaxies with a potential counterpart}}}{N_{\text{simulated galaxies}}} N_{\text{galaxies in survey region}} \quad (\text{B2})$$

We note that galaxies with low fluxes or large extents often have higher positional errors than bright and/or compact galaxies; the positional uncertainty of a given source is roughly the gridded Parkes beam, 15.5', divided by the signal-to-noise. The

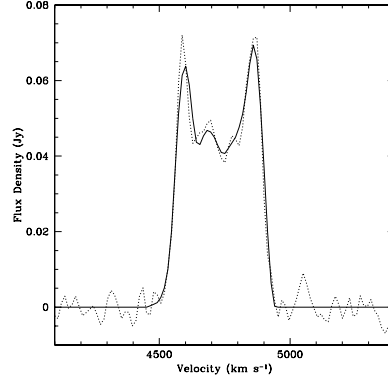


FIG. A1.— Spectrum (dotted line) and Savitzky-Golay smoothed profile (solid line) of J1853+09.

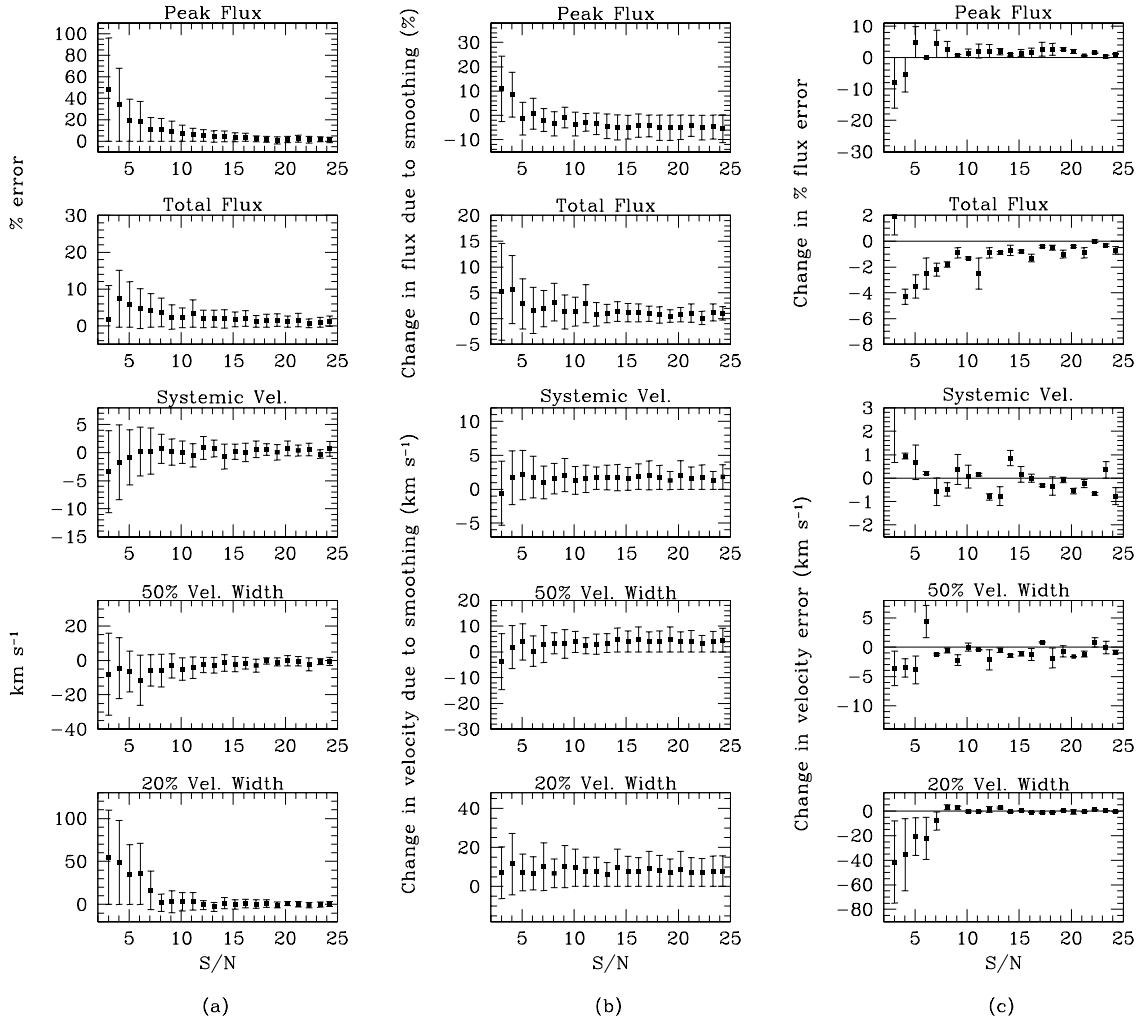


FIG. A2.— (a) The errors on measured HI parameters for the template as a function of S/N; (b) the difference between the parameters of the smoothed simulated profiles and the original parameters of the template; (c) the difference between the absolute value of the HI errors measured from the simulated spectra and those measured from the template. The points represent the median errors and the error bars (in both the +y and -y directions) represent the median absolute value of the errors.

TABLE B1  
RESULTS OF AUTOMATED SEARCH FOR MULTIWAVELENGTH COUNTERPARTS

	Optical	2MASS	IRAS
$l = 36^\circ$ to $52^\circ$ , $\Delta r \leq 5'$ :			
$N_{\text{counterparts}}$ found via automated search	2	6	24
% expected to be real	5%	77%	18%
$N_{\text{counterparts}}$ that remain after visual inspection <sup>a</sup>	1(50%)	4(67%)	2(8%)
$l = 36^\circ$ to $52^\circ$ , $\Delta r \leq 3'$ :			
$N_{\text{counterparts}}$ found via automated search with $\Delta r \leq 3'$	1	5	14
% expected to be real	26%	88%	35%
$N_{\text{counterparts}}$ that remain after visual inspection <sup>a</sup>	1(100%)	3(60%)	2(14%)
$l = 196^\circ$ to $212^\circ$ , $\Delta r \leq 5'$ :			
$N_{\text{counterparts}}$ found via automated search	17	31	15
% expected to be real	96%	59%	52%
$N_{\text{counterparts}}$ that remain after visual inspection <sup>a</sup>	17(100%)	16(52%)	9(60%)
$l = 196^\circ$ to $212^\circ$ , $\Delta r \leq 3'$ :			
$N_{\text{counterparts}}$ found via automated search with $\Delta r \leq 3'$	14	26	13
% expected to be real	96%	79%	78%
$N_{\text{counterparts}}$ that remain after visual inspection <sup>a</sup>	14(100%)	14(54%)	9(69%)

<sup>a</sup>#(%) gives the number and percentage of counterparts found via the automated search that remain on our list of likely counterparts (and are therefore in Table 3) following a visual inspection of all possible counterparts. In seven cases, the most likely 2MASS counterpart was not the nearest 2MASS counterpart to the HI position, and therefore was not the one found during our automated search. DSS galaxies were also not found via the automated search, nor was PGC 3097165.

probabilities given by these simulations are for the entire sample; the above effect will cause slight variations among individual galaxies. The simulations were run separately for the two regions of the survey as the density and therefore reliability of counterparts is field-dependent. The difference between simulations with different degrees of clustering around the real HI sample was used to evaluate the approximate errors on the estimated counterpart likelihoods,  $P$ ,  $\sim \pm 10\%$ .

We present in Table B1 the results of the counterpart likelihood simulations. The percentage of counterparts found via the automated search that were still considered likely after a visual verification is roughly consistent with the expected percentages calculated by means of the simulations. The number of likely counterparts to the galaxies in the  $l = 196^\circ$  to  $212^\circ$  region is substantially higher than that of the galaxies in the  $l = 36^\circ$  to  $52^\circ$  region. The difference between the number of potential counterparts in the two survey regions can be attributed to the lower extinction in the latter field. Using the  $100 \mu\text{m}$  DIRBE/IRAS data (Schlegel et al. 1998), we calculate mean B-band extinctions of  $12^{\text{m}}.0$  and  $3^{\text{m}}.2$  over the  $l = 36^\circ$  to  $52^\circ$  and  $l = 196^\circ$  to  $212^\circ$  regions, respectively. This point is further illustrated by the E(B-V) contours plotted on Figure 8. Although this data are not well calibrated in the Galactic plane, they are still useful for general comparison purposes.

## REFERENCES

- Barnes, D. G. et al. 2001, MNRAS, 322, 486  
Fairall, A. P. 1998, *Large-Scale Structures in the Local Universe*, (Chichester: Wiley)  
Freeman, K. C., Karlsson, B., Lynga, G., Burrell, J. F., van Woerden, H., Goss, W. M., & Mebold, U. 1977, A&A, 55, 445  
Giovannelli, R. 1979, ApJ, 227, L125  
Giovannelli, R., & Haynes, M. P. 1981, AJ, 86, 340  
Gooch, R. E. 1995, in ASP Conf. Ser. 101, *Astronomical Data Analysis Software and Systems V*, ed. G. H. Jacoby, & J. Barnes (San Francisco: ASP), 80  
Henning, P. A. 1992, ApJS, 78, 365  
Henning, P. A., Kraan-Korteweg, R. C., Rivers, A. J., Loan, A. J., Lahav, O., & Burton, W. B. 1998, AJ, 115, 584 [Dw]  
Henning, P. A. et al. 2000, AJ, 119, 2686 [HIZSS]  
Jarrett, T.-H., Chester, T., Cutri, R., Schneider, S., Rosenberg, J., Huchra, J. P., & Mader, J. 2000, AJ, 120, 298  
Juraszek, S. J. et al. 2000, AJ, 119, 1627  
Karachentsev, I., & Musella, I. 1996, A&A, 315, 348  
Kilborn, V. A. 2000, Ph.D. Thesis, University of Melbourne  
Kilborn, V. A. et al. 2002, AJ, 124, 690  
Kolatt, T., Dekel, A., & Lahav, O. 1995, MNRAS, 275, 797  
Koribalski, B. S. et al. 2004, AJ, 128, 16  
Kraan-Korteweg, R. C., Loan, A. J., Burton, W. B., Lahav, O., Ferguson, H. C., Henning, P. A., & Lynden-Bell, D. 1994, Nature, 372, 77  
Kraan-Korteweg, R. C., Koribalski, B. S., & Juraszek, S. 1999, in ESO/ATNF Workshop on "Looking Deep in the Southern Sky", eds. F. Morganti & W. Couch, Springer, 23  
Kraan-Korteweg, R. C. 2000, A&AS, 141, 123  
Kraan-Korteweg, R. C., & Lahav, O. A&ARv, 2000, 10, 211  
Lercher, G., Kerber, F., & Weinberger, R. 1996, A&AS, 117, 369  
Maffei, P. 1968, PASP, 80, 618  
Meyer, M. J. et al. 2004, MNRAS, 350, 1195  
Michel, A., & Huchra, J. 1988, PASP, 100, 1423  
Nakanishi, K., Takata, T., Yamada, T., Takeuchi, T. T., Shiroya, R., Miyazawa, M., Watanabe, S., & Saito, M. 1997, ApJS, 112, 245  
Nilson, P. 1973, Uppsala General Catalog of Galaxies (Uppsala: Astron. Obs.) [UGC]  
Ostriker, E. C., Huchra, J. P., Geller, M. J., & Kurtz, M. J. 1988, AJ, 96, 1775  
Pantoja, C. A., Giovanardi, C., Altschuler, D. R., & Giovanelli, R. 1994, AJ, 108, 921  
Pantoja, C. A., Altschuler, D. R., Giovanardi, C., & Giovanelli, R. 1997, AJ, 113, 905 [CAP]  
Press et al. 1992, *Numerical recipes in C: The Art of Scientific Computing*, 2nd edition, (Cambridge: Cambridge University Press)  
Rivers, A. J. 2000, Ph.D. Thesis, University of New Mexico [Dw]  
Roman, A. T. Iwata, I., & Saito, M. 2000, ApJS, 127, 27  
Rosenberg, J. L., & Schneider, S. E. 2000, ApJS, 130, 177 [ADBS]  
Rosenberg, J. L., & Schneider, S. E. 2002, ApJ, 567, 247  
Roth, J., Mould, J., & Staveley-Smith, L. 1994, AJ, 108, 851  
Ryan-Weber, E. et al. 2002, AJ, 124, 1954  
Sault, R. J., Teuben, P. J., & Wright, M. C. H. 1995, in ASP Conf. Ser. 77, *Astronomical Data Analysis Software and Systems IV*, ed. R. A. Shaw, H. E. Payne, & J. J. E. Hayes (San Francisco:ASP), 433  
Saunders, W., Rowan-Robinson, M., Lawrence, A., Efstathiou, G., Kaiser, N., Ellis, R. S., & Frenk, C. S. 1990, MNRAS, 242, 318  
Schechter, P. L. 1976, ApJ, 203, 297  
Schlegel, D. J., Finkbeiner, D. P., & Davis, M. 1998, ApJ, 500, 525  
Schmidt, M. 1968, ApJ, 151, 393  
Schröder, A., Kraan-Korteweg, R. C., & Mamon, G. A. 1999, PASA, 16, 42  
Seeberger, R., Saurer, W., & Weinberger, R. 1996, A&AS, 117, 1 [ZOAG]

- Staveley-Smith, L. et al. 1996, PASA, 13, 243  
 Theureau, G., Bottinelli, L., Coudreau-Durand, N., Gouguenheim, L., Hallet, N., Loulergue, M., Paturel, G., & Teerikorpi, P. 1998, A&AS, 130, 333  
 Thuan, T. X., & Seitzer, P. O. 1979, ApJ, 231, 680  
 Weinberger, R. 1980, A&AS, 40, 123 [WEIN]  
 Woudt, P. A., & Kraan-Korteweg, R. C. 2001, A&A, 380, 441  
 Zwaan, M. A., Briggs, F. H., Sprayberry, D., & Sorar, E. 1997, ApJ, 490, 173  
 Zwaan, M. A. et al. 2003, AJ, 125, 2842

TABLE 1  
HI AND DERIVED PROPERTIES

HIZOA	$\alpha_{2000}$	$\delta_{2000}$	$\ell$	$b$	Flux <sup>a</sup> (Jy km s <sup>-1</sup> )	V (cz) (km s <sup>-1</sup> )	50% Vel. Width (km s <sup>-1</sup> )	20% Vel. Width (km s <sup>-1</sup> )	LG Distance (Mpc)	Log HI Mass (M <sub>☉</sub> )
J0608+13	06 08 30	13 05 34	196.38	-3.34	2.27±0.14	5645±4	50±8	65±4	74	9.5
J0614+12	06 14 60	12 31 06	197.65	-2.22	4.03±0.22	5553±2	217±7	237±8	73	9.7
J0615+11	06 15 40	11 09 54	198.92	-2.72	7.67±0.28	5446±5	184±14	238±12	71	10.0
J0621+11	06 21 34	11 09 18	199.61	-1.45	7.74±0.20 <sup>b</sup>	5599±2	188±5	226±7	73	10.0
J0621+10	06 21 44	10 25 39	200.27	-1.75	6.74±0.27	7467±6	173±12	265±40	98	10.2
J0622+06	06 22 04	06 29 49	203.79	-3.52	8.34±0.64	3598±7	296±17	314±23	46	9.6
J0622+11A	06 22 05	11 22 22	199.48	-1.23	2.43±0.64 <sup>b</sup>	5669±7	41±17	66±23	74	9.5
J0622+04	06 22 29	04 31 57	205.58	-4.34	7.74±0.22	2958±3	306±12	367±15	38	9.4
J0622+11B	06 22 59	11 08 09	199.79	-1.15	19.08±0.24 <sup>b</sup>	5493±1	366±2	409±4	72	10.4
J0623+14	06 23 19	14 43 41	196.66	0.60	5.44±1.02	5308±17	286±44	330±84	70	9.8
J0623+09	06 23 27	09 29 46	201.29	-1.82	6.27±0.27	8151±10	238±35	343±20	107	10.2
J0623+04	06 23 36	04 22 55	205.84	-4.17	3.30±0.19	2870±3	97±9	130±10	37	9.0
J0625+03	06 25 41	03 48 53	206.59	-3.97	4.80±0.22	6219±3	234±11	324±41	81	9.9
J0626+05	06 26 08	05 01 09	205.57	-3.31	2.67±0.11	3595±5	103±7	149±7	46	9.1
J0630+16	06 30 05	16 50 37	195.54	3.03	30.26±0.62	2532±3	258±8	328±9	33	9.9
J0630+08	06 30 09	08 22 37	203.06	-0.87	4.92±0.29	367±1	33±4	55±5	3	7.0
J0630+02	06 30 42	02 40 38	208.18	-3.38	3.59±0.13	2774±3	120±6	144±5	35	9.0
J0632+06	06 32 53	06 17 16	205.22	-1.24	3.28±0.21	3147±6	117±19	168±10	40	9.1
J0633+10	06 33 59	10 40 40	201.45	1.03	1.68±0.09	7547±2	43±3	65±6	99	9.6
J0634+09	06 34 05	09 13 17	202.76	0.38	1.29±0.10	3876±1	37±5	48±5	50	8.9
J0634+00	06 34 20	00 03 37	210.93	-3.78	1.88±0.11	6183±2	56±5	86±7	80	9.5
J0635+14A	06 35 17	14 59 15	197.77	3.29	6.44±0.15	3827±4	275±11	328±11	50	9.6
J0635+02	06 35 44	02 24 17	209.00	-2.39	4.07±0.33	6334±14	41±23	228±41	83	9.8
J0635+03	06 35 51	03 09 45	208.34	-2.02	1.49±0.19	2832±3	33±8	59±12	36	8.7
J0635+11	06 35 54	11 09 44	201.24	1.67	9.11±0.30	3734±5	408±9	479±5	48	9.7
J0635+14B	06 35 54	14 36 21	198.18	3.25	16.47±0.13	4020±1	329±2	360±2	52	10.0
J0636+00	06 36 24	00 56 42	210.37	-2.91	17.39±0.16	2723±1	144±2	188±3	34	9.7
J0636+04	06 36 51	04 03 60	207.65	-1.38	5.45±0.24	3520±4	185±13	196±22	45	9.4
J0637+03	06 37 39	03 24 13	208.33	-1.51	5.93±0.35	3431±3	160±7	172±7	44	9.4
J0641+01	06 41 03	01 50 60	210.10	-1.47	6.78±0.19	2795±2	181±5	199±4	35	9.3
J0643+06	06 43 18	06 57 57	205.81	1.37	7.75±0.32	6903±3	356±9	381±12	90	10.2
J0644+12	06 44 01	12 25 58	201.01	4.02	9.34±0.26	3925±2	403±6	425±15	51	9.8
J0649+09	06 49 35	09 43 03	204.06	4.01	15.92±0.30	7513±3	268±15	302±8	99	10.6
J0653+07	06 53 42	07 09 54	206.80	3.76	5.63±0.24	7035±4	329±6	360±32	92	10.1
J0654+08	06 54 10	08 35 36	205.58	4.51	5.79±0.15	2625±4	128±9	172±9	33	9.2
J0656+06A	06 56 26	06 01 44	208.13	3.85	12.29±0.21 <sup>b</sup>	6391±3	184±6	228±4	83	10.3
J0656+06B	06 56 28	06 16 43	207.91	3.97	10.69±0.21 <sup>b</sup>	6784±5	207±9	286±14	89	10.3
J0659+06	06 59 37	06 26 15	208.12	4.74	4.38±0.18	6365±3	145±7	168±8	83	9.9
J0700+01	07 00 58	01 56 04	212.30	3.00	15.06±0.32	1762±1	334±3	360±3	21	9.2
J0702+04	07 02 24	04 52 39	209.83	4.66	7.23±0.23	6934±3	241±5	263±6	90	10.1
J0702+03	07 02 50	03 13 37	211.35	4.00	4.20±0.26	3551±3	86±10	121±20	45	9.3
J0705+02	07 05 39	02 37 37	212.21	4.36	5.17±0.15	1745±1	34±2	49±2	21	8.7
J1843+06	18 43 42	06 33 59	37.91	4.70	6.34±0.47	8918±6	266±18	304±31	121	10.3
J1852+10	18 52 59	10 25 49	42.41	4.40	5.17±0.16	4906±4	238±12	275±7	68	9.8
J1853+09	18 53 49	09 51 11	41.98	3.95	18.30±0.27	4729±1	320±3	350±3	66	10.3
J1855+07	18 55 22	07 38 34	40.18	2.61	6.08±0.42	6159±4	266±11	330±36	85	10.0
J1857+13	18 57 22	13 26 26	45.59	4.80	5.01±0.30	8095±5	173±20	...	111	10.2
J1900+13	19 00 06	13 33 21	45.99	4.25	9.40±0.24	4658±2	234±4	252±7	65	10.0
J1901+06	19 01 40	06 51 44	40.20	0.86	17.27±0.17	2945±1	61±2	88±1	42	9.9
J1904+03A	19 04 15	03 06 47	37.16	-1.43	5.60±0.22 <sup>b</sup>	3289±2	76±5	125±9	46	9.5
J1904+03B	19 04 27	03 11 32	37.26	-1.43	5.53±0.33 <sup>b</sup>	3195±4	232±15	260±9	45	9.4
J1906+12	19 06 13	12 57 17	46.13	2.66	8.47±0.36	2730±2	267±6	293±20	39	9.5
J1906+07	19 06 53	07 33 52	41.42	0.04	5.16±0.30	3095±5	138±12	188±18	44	9.4
J1907+14	19 07 33	14 02 54	47.26	2.87	4.18±0.29	7290±3	89±10	...	100	10.0
J1908+05	19 08 26	05 59 34	40.20	-1.03	5.97±0.28	4567±4	168±9	196±14	63	9.8
J1910+00	19 10 25	00 33 28	35.60	-3.97	16.60±0.36	1494±1	180±5	194±4	22	9.3
J1912+13	19 12 39	13 24 33	47.26	1.48	7.09±0.15	2774±1	102±3	117±2	40	9.4
J1912+02	19 12 45	02 56 32	37.99	-3.39	15.23±0.42	6541±10	470±22	597±20	90	10.5
J1913+17	19 13 49	17 35 31	51.10	3.16	2.58±0.20	4726±4	80±11	124±9	66	9.4
J1913+16	19 13 59	16 54 60	50.52	2.81	11.47±0.67	6263±4	539±9	616±22	87	10.3
J1914+10	19 14 57	10 17 47	44.76	-0.47	20.66±0.37	654±0	66±2	83±2	12	8.8
J1917+07	19 17 27	07 49 14	42.86	-2.17	6.89±0.19	3033±2	226±6	243±6	43	9.5
J1917+04	19 17 38	04 26 33	39.89	-3.78	11.18±0.33	6330±10	325±22	416±11	87	10.3
J1918+16	19 18 38	16 10 13	50.38	1.48	7.08±0.35	6639±13	165±37	279±17	92	10.1
J1919+14	19 19 59	14 04 01	48.67	0.20	13.70±0.44	2809±2	137±7	195±8	40	9.7
J1921+14	19 21 36	14 54 26	49.60	0.25	6.56±0.22	4080±2	72±5	88±6	57	9.7
J1921+08	19 21 59	08 16 59	43.79	-2.94	5.97±0.39	3115±4	100±10	125±15	44	9.4
J1926+08	19 26 02	08 16 09	44.25	-3.84	2.62±0.18	3088±2	67±11	113±15	44	9.1
J1927+12	19 27 36	12 19 20	48.01	-2.25	5.38±0.38	8604±6	138±17	204±15	118	10.2
J1927+09	19 27 57	09 26 51	45.52	-3.70	1.69±0.22	7920±4	48±7	77±24	108	9.7
J1929+08	19 29 18	08 03 55	44.46	-4.64	19.08±0.97	3097±6	195±13	341±14	44	9.9
J1929+11	19 29 24	11 36 44	47.59	-2.98	5.78±0.31	6331±6	351±16	388±12	87	10.0
J1930+12	19 30 29	12 12 07	48.24	-2.93	6.07±0.28	6684±3	213±11	240±13	92	10.1



TABLE 1 — *Continued*

HIZOA	$\alpha_{2000}$	$\delta_{2000}$	$\ell$	$b$	Flux <sup>a</sup> (Jy km s <sup>-1</sup> )	V (cz) (km s <sup>-1</sup> )	50% Vel. Width (km s <sup>-1</sup> )	20% Vel. Width (km s <sup>-1</sup> )	LG Distance (Mpc)	Log HI Mass (M <sub>⊙</sub> )
J1930+11	19 30 36	11 18 53	47.47	-3.38	3.11±0.16	3174±3	108±7	124±11	45	9.2
J1933+10	19 33 56	10 42 35	47.33	-4.39	6.67±0.35	5255±3	240±8	282±9	73	9.9
J1937+14	19 37 12	14 42 55	51.23	-3.15	3.20±0.15	4485±2	59±4	74±5	63	9.5
J1940+11	19 40 36	11 54 18	49.18	-5.24	1.49±0.17	580±2	20±5	32±11	11	7.6

<sup>a</sup> The error we estimate for the integrated flux does not take into account the uncertainty due to baseline subtraction or the uncertainty in calibration; the total error on the integrated flux is likely to be  $\sim 10$ -15%

<sup>b</sup> The flux was calculated over a smaller region to isolate the galaxy emission from that arising from a nearby galaxy. This may have led to an underestimation of the total flux.

<sup>c</sup> The 20% velocity width could not be accurately measured.

TABLE 2  
MULTIWAVELENGTH COUNTERPARTS

Name	b	E(B-V) <sup>a</sup>	HI Counterpart	Sep ( <sup>′</sup> )	$\Delta v^b$ (km s <sup>-1</sup> )	Optical Counterpart <sup>c</sup>	Sep ( <sup>′</sup> )	2MASS Counterpart <sup>c</sup> (2MASX)	Sep ( <sup>′</sup> )	IRAS Counterpart <sup>c</sup> (IRAS)	Sep ( <sup>′</sup> )
J0615+11	-2.72	0.8	ADBS J061543+1110	1.4	9.4	DSS galaxy	...	J06154496+1110227	1.3	...	...
J0621+11	-1.45	0.9	...	...	...	ZOAG G199.66-01.50	4.2	J06212888+1105105	4.2	...	...
J0621+10	-1.75	0.7	CAP 0618+10	1.0	6.1	WEIN 192	1.0	J06214000+1024565	1.0	06188+1026	1.0
J0622+06	-3.52	0.5	...	...	...	ZOAG G203.78-03.50	1.7	J06220859+0631063	1.7	06194+0632	2.0
J0622+11A	-1.23	0.9	...	...	...	DSS galaxy	4.0	...	...	...	...
J0622+04	-4.34	0.6	CAP 0619+04	0.9	4.9	ZOAG G205.58-04.36	0.9	J06222633+0431236	0.9	06197+0432	0.8
J0622+11B	-1.15	1.1	ADBS J062302+1108	1.1	50.0	DSS galaxy	...	J06225815+1108312	0.4	06202+1109	0.9
J0623+14	0.60	0.9	WEIN 179	1.7	54.3	WEIN 179	1.7	J06231132+1443129	1.7	...	...
J0623+09	-1.82	0.6	...	...	...	DSS galaxy	...	J06233278+0930182	1.8	...	...
J0625+03	-3.97	0.6	...	...	...	see note <sup>d</sup>	...	see note <sup>d</sup>	...	...	...
J0630+16	3.03	0.6	...	...	...	ZOAG G195.62+03.04	4.7	J06301575+1646422	4.7	...	...
J0630+02	-3.38	0.9	...	...	...	DSS galaxy	...	J06303567+0238356 <sup>e</sup>	2.4	...	...
J0633+10	1.03	1.5	...	...	...	...	...	J06334997+1039414	2.4	...	...
J0634+09	0.38	0.8	...	...	...	DSS galaxy	0.4	...	...	...	...
J0635+14A	3.29	0.5	UGC 03498	1.0	-27.3	UGC 03498	1.0	J06352031+1458436	0.9	06324+1501	1.0
J0635+02	-2.39	1.8	...	...	...	DSS galaxy	...	J06353276+0224228	2.6	...	...
J0635+11 <sup>f</sup>	1.67	1.5	ADBS J063549+1107	2.4	31.3	DSS galaxy	1.6	...	...	...	...
...	...	...	ADBS J063606+1109	2.4	-163.8	...	...	...	...	...	...
J0635+14B	3.25	0.6	...	...	...	PGC 3097165	0.8	J06355671+1435584	0.7	...	...
J0636+00	-2.91	1.5	...	...	...	ZOAG G210.39-02.92	1.0	...	...	06338+0058	0.9
J0643+06	1.37	0.8	WEIN 206	1.4	2.4	WEIN 206	1.4	J06431155+0657324	1.4	...	...
J0644+12	4.02	0.4	UGC 03524	1.9	-2.9	UGC 03524	1.9	J06440058+1224067	1.9	06412+1227	1.8
J0649+09	4.01	0.3	...	...	...	ZOAG G204.10+03.97	3.4	J06493148+0939437	3.4	...	...
J0653+07	3.76	0.3	...	...	...	ZOAG G206.80+03.71	2.8	J06533152+0708263	2.8	...	...
J0654+08	4.51	0.2	ADBS J065406+0834	1.4	13.9	ZOAG G205.59+04.48	1.4	...	...	...	...
J0656+06A	3.85	0.4	CAP 0653+06	1.9	-0.3	ZOAG G208.14+03.82	1.9	J06562110+0600057	1.9	...	...
J0656+06B	3.97	0.3	UGC 03607	2.4	-18.0	UGC 03607	2.4	J06561786+0616066	2.4	06536+0620	2.3
J0659+06	4.74	0.3	...	...	...	DSS galaxy <sup>g</sup>	1.1	...	...	...	...
J0700+01	3.00	0.5	UGC 03630	1.9	-0.4	UGC 03630	1.9	J07010328+0154406	1.9	06584+0158	2.0
J0702+04	4.66	0.3	CAP 0659+04	1.6	-3.9	ZOAG G209.84+04.63	1.6	J07021916+0451191	1.6	...	...
J0702+03	4.00	0.4	...	...	...	DSS galaxy	2.4	...	...	...	...
J0705+02	4.36	0.5	[H92] 16	0.3	0.3	...	...	...	...	...	...
J1857+13	4.80	0.9	...	...	...	DSS galaxy	...	J18573802+1328565	4.8	...	...
J1901+06	0.86	5.6	Dw040.0+0.9	1.3	-10.5	...	...	...	...	...	...
J1906+12	2.66	1.5	2MASX J19061820+1256195	1.6	-8.4	DSS galaxy	...	J19061820+1256195	1.6	...	...
J1910+00	-3.97	0.7	HIZSS 110	3.0	9.0	...	...	...	...	...	...
J1913+16	2.81	2.4	...	...	...	DSS galaxy	...	J19135226+1655279	1.5	...	...
J1914+10	-0.47	11.7	Dw044.8-0.5	0.3	15.5	...	...	...	...	...	...
J1917+07	-2.17	1.9	...	...	...	DSS galaxy	0.5	...	...	...	...
J1917+04	-3.78	1.0	ZOAG G039.88-03.78	0.1	7.2	ZOAG G039.88-03.78	0.1	J19173769+0426248	0.1	19151+0421	0.2
J1929+08	-4.64	0.5	...	...	...	DSS galaxy	1.3	...	...	19269+0756	1.3
J1933+10	-4.39	0.5	...	...	...	DSS galaxy	...	J19335171+1042247	0.8	...	...

<sup>a</sup> from DIRBE/IRAS 100  $\mu$ m extinction maps (Schlegel et al. 1998)

<sup>b</sup>  $\Delta v = v_{\text{counterpart}} - v \text{ (km s}^{-1}\text{)}$

<sup>c</sup> The references for counterparts are as follows: (ADBS) Rosenberg & Schneider 2000; (CAP) Pantoja et al. 1997; (Dw) Henning et al. 1998, Rivers 2000; (HIZSS) Henning et al. 2000; (PGC) <http://leda.univ-lyon1.fr/>; (UGC) Nilson 1973; (WEIN) Weinberger 1980; (ZOAG) Seeberger, Saurer, & Weinberger 1996; (2MASX) J19061820+1256195) Jarrett et al. 2000

<sup>d</sup> There are two possible counterparts to this source, 2MASS J06254183+0346338 at a separation of 2.3<sup>′</sup> and a DSS galaxy at  $\alpha = 06^{\text{h}}25^{\text{m}}45^{\text{s}}.1$ ,  $\delta = 03^{\circ}47'55''$  (separation = 1.4<sup>′</sup>). We do not have enough information to decide between the two.

<sup>e</sup> We note that there is another possible 2MASS counterpart, J06303033+0240026, at a separation of 2.7<sup>′</sup>. This candidate appears to be of earlier type than that chosen above, but can not be excluded.

<sup>f</sup> Our HI detection was resolved into two galaxies separated by 4<sup>′</sup> by the ADBS. We are unable to say to which HI galaxy the counterpart belongs.

<sup>g</sup> In addition to the counterpart listed here, we see another DSS galaxy at  $\alpha = 06^{\text{h}}59^{\text{m}}38^{\text{s}}.1$  and  $\delta = 06^{\circ}25'19''$  as well as two 2MASS candidates: J06595034+0623322 (sep=4.3<sup>′</sup>) and J06595034+0623322 (sep=4.4<sup>′</sup>). From morphology and separation arguments, we believe the candidate we have chosen is the most likely, but we can not rule out those listed here.